Title: Spatial periodicity of hippocampal place cells in navigation

Bo Zhang[1,2], and Jia Liu[2*]

[1] Beijing Academy of Artificial Intelligence, Beijing, 100084, China

[2] Tsinghua Laboratory of Brain and Intelligence & Department of Psychology, Tsinghua University, Beijing, 100084, China

*Correspondence shall be addressed to: JL, liujiathu@tsinghua.edu.cn

Abstract

To achieve the computational goal of navigating both natural and mental spaces, the brain employs a cognitive map, which hippocampal place cells actualize to encode locations of the map using a hexagonal coordinate system provided by entorhinal grid cells. However, how this map is leveraged for navigational tasks remains unclear. Here, we designed an object-matching task where participants unknowingly manipulated object variants spatially arranged in a ring-like structure around a prototype. Functional neuroimaging revealed a spatial 3-fold periodicity in hippocampal activity during navigation, replicated across different groups. Importantly, this hippocampal periodicity was phase-locked with the well-documented 6-fold periodicity of entorhinal cortex, suggesting a holistic functional coupling between these regions. In light of this empirical evidence, we developed the E-H PhaseSync Model, which incorporates an algorithm formalizing the interplay of place cells' forward replay and grid cells' spatial axes, thereby generating a 3-fold periodic hippocampal vector field serving as a navigational guide. The implementation of the model not only reproduced participants' navigational behavior but also surprisingly predicted a 3-fold periodicity embedded in the behavior, which was substantiated by participants' behavioral data. Taken together, this study suggests that spatial periodicity originating from entorhinal grid cells serves as a bond to consolidate the hippocampal-entorhinal network, where the periodic hippocampal vector field emerges as the neural basis for utilizing the cognitive map in navigation.

Introduction

The Cognitive map (Tolman, 1948), encoded by hippocampal place cells, is a mental representation of both spatial and conceptual relationships and hierarchies (O'Keefe & Dostrovsky, 1971; Epstein et al., 2017; Behrens et al., 2018; Bottini & Doeller, 2020). Thus, it serves as a cognitive framework for understanding connections between different pieces of information, thereby facilitating knowledge retrieval and decision-making predicated on these relationships (Park et al., 2020; Toledo et al., 2020; Nyberg et al., 2022; De Cothi et al., 2022; Muhle-Karbe et al., 2023). However, in practical navigation tasks, how abstract relations are actualized by hippocampal place cells to perform path integration remains unclear. A recent study (Ormond and

O'Keefe, 2022) sheds light on this issue by unveiling the convergence sinks (ConSinks) of hippocampal place cells, which are vector fields encoding allocentric directions and distances distributed across environment and exhibit maximal activity when mice orient towards the goal. This finding underscores the hippocampal place cells in providing vector-based representations as navigational signals to reach the intended goal. In this study, we investigated how hippocampal vector fields, that represent the direction from self-location to the goal, are constructed during navigation.

Anatomically, the hippocampus (HPC) received major projections from the upstream entorhinal cortex (ERC) (Witter & Amaral, 1991; van Groen et al., 2003; Garcia and Buffalo, 2020), and complete lesions of the ERC result in a substantial disruption of place representation in precision and stability (Hales et al., 2014). The grid cells, which reside in the ERC (Hafting et al., 2005) and exhibit a characteristic hexagonal firing pattern creates a metric for space, have been proposed by computational models to be the foundation for place field formation through the phase vector of multi-scale grid modules (Solstad et al., 2006; de Almeida et al., 2009; Bush et al., 2014; Bush et al., 2015; Bicanski and Burgess, 2019). Grid cells were also empirically found to track direction and velocity essential for navigation (Sargolini et al., 2006; Munn et al., 2020; Gerlei et al., 2020; Morris & Derdikman, 2023). Those evidences support the possibility that grid cells might serve as the geometric framework with periodic codes, which pomotes the formation of hippocampal vector fields of place cells via the ERC-HPC circuitry. The examination of this idea requires simultaneously recording neural activity of both ERC and HPC at the populational level, we thus used fMRI, which offers a broader scope of brain scanning relative to electrophysiology, to examine whether there is spatial periodicity in the HPC and more critically whether this spatial periodicity, if observed, is phase-locked to the spatial periodicity of the ERC. Fortunately, the orientation and spacing of grid cells remain almost invariant at populational level (Hafting et al., 2005; Stensola et al., 2015; Krupic et al., 2015; Gardner et al., 2022). If the 6-fold periodicity of grid cell populations could be detected by fMRI (Doeller et al., 2010; Constantinescu et al., 2016; Bao et al., 2019; Wagner et al., 2023; Raithel et al., 2023), it is possible that spatial periodicity may also be present in the hippocampus at the population level during navigation.

To investigate this, we developed an object matching task, which required participants to morph the object variants by button press to match the target prototype by navigating in a 2-dimensional object space (Fig. 1). To explore potential spatial periodicity in the HPC, the starting locations were arranged in a ring-shaped pattern, with each location corresponded to a unique conceptual direction towards the goal ranging from 0° to 360°. Spectral analysis revealed a spatial periodicity of 3-fold modulation in the CA1 of HPC, whose phase was closely coupled with the spatial periodicity of 6-fold modulation in the ERC. Based on this empirical finding, we built the "E-H PhaseSync" model to explain how hippocampal vector fields were formed from the hexagonal firing pattern of grid cells.

Results

Construction of a conceptual object space

A novel 3D object, named greeble (Gauthier and Tarr, 1997; Fig.1a), was used to construct a conceptual object space. Within this space, each location in the space (Fig.1c) represented a unique greeble variant characterized by distinct length of its two components, namely "Loogit" and "Vacso," that form the two dimensions of the space. The greeble in the center of the space was the prototype, serving as the target. In each trial, a greeble variant, randomly selected from the periphery of the space (Fig.1c, the red point within the ring-shaped orange area), was presented on screen. Participants adjusted the length of Loogit and Vasco independently via button press to match the prototype as accurately as possible (Fig.1b). This process generated a navigational trajectory constituted by a sequence of selected greeble variants (i.e., locations; Fig.1c). To ensure comprehensive exploration of the object space, greeble variants were evenly sampled such that participants experienced conceptual directions ranged from 0° to 360° relative to the goal location (see Methods for details). Note that no participant was aware of the existence of the object space or had a subjective feeling of navigating during the experiment. To mitigate the impact of learning effects on BOLD signal series of MRI scanning, participants were trained one day prior to the MRI experiment (see Fig.S1 for details). As a result, all participants performed the task well, and the probability density map of the ending-locations across trials had a peak at the prototype (Fig. 1d).

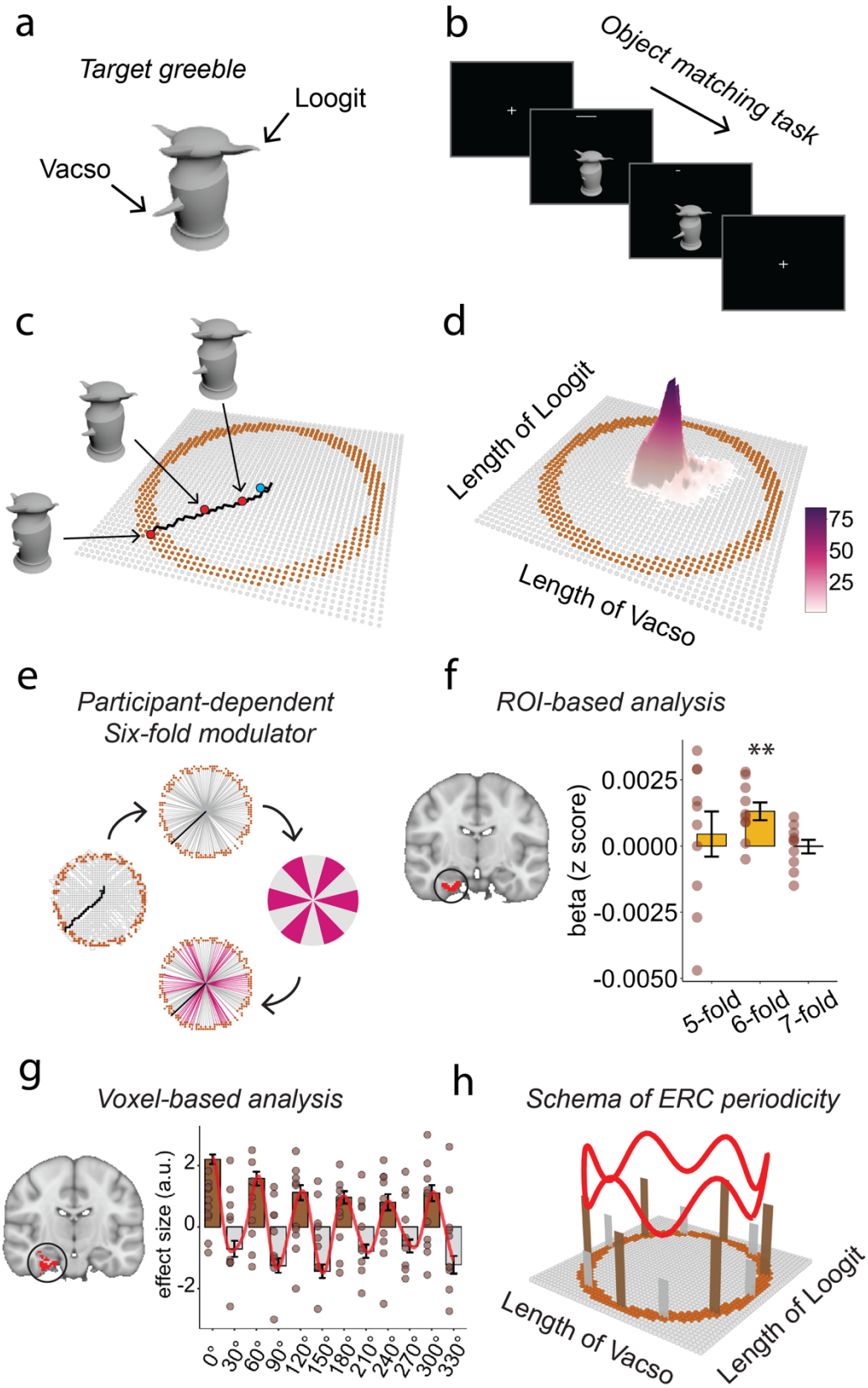
a
Target greeble
Loogit
Vacso
b
Object matching task
c
d
Length of Loogit
Length of Vacso
75
50
25
e
Participant-dependent
Six-fold modulator
f
ROI-based analysis
**
0.0025
0.0000
-0.0025
-0.0050
beta (z score)
5-fold
6-fold
7-fold
g
Voxel-based analysis
effect size (a.u.)
2
0
-2
0°
30°
60°
90°
120°
150°
180°
210°
240°
270°
300°
330°
h
Schema of ERC periodicity
Length of Vacso
Length of Loogit

Figure 1. Experimental design and 6-fold modulation in the Entorhinal cortex. a) Depiction of the greeble prototype and its two defining components, namely "Loogit" and "Vacso." b) Within the MRI scanner, participants continuously adjusted the length of Loogit and Vacso to match the prototype by button press within a 10-s time limit. c) Conceptual object space. Each orange dot within the ring-shaped area represents a variant greeble, while the central blue dot indicates the prototype greeble (i.e., the goal location). Red dots denote intermediate locations along the navigational trajectory (i.e., the black line). d) Distribution of the ending-locations, aggregated across participants. e) Schematic detailing the six-fold modulator for localizing grid cell activity. Participants' trajectories were simplified to straight lines connecting the starting and the ending locations, which were further classified into either "aligned" or "misaligned" conditions. For each participant's individual trajectories, see Fig. S2. f) ROI-based analysis, with an anatomical mask manually delineated from the MNI template, replicated the 6-fold modulation of BOLD signal series in comparison to both 5- and 7-fold modulations. g) Voxel-based sinusoid analysis revealed grid cell activity within the right ERC (peak MNI coordinate: 19, -15, -27; peak $t = 4.58$). h) Three-dimensional schema illustrating the relationship between the 6-fold modulation in the ERC and conceptual directions within the object space.

Six-fold modulation in the ERC and 3-fold modulation in the HPC

In the fMRI analysis, we first identified the entorhinal hexagonal activity when participants implicitly navigated in the object space. With the sinusoidal analysis (Fig.1e, see Methods for details), we revealed a significant deviation from uniform grid orientations (Fig.S3, $p < 0.05$, Rayleigh test of uniformity, Bonferroni corrected), and identified a significant activity cluster in the right ERC (Fig.1g; $p < 0.01$, initial threshold; $p < 0.05$, small-volume cluster-corrected (SVC) for multiple comparisons; Cohen's $d = 0.7$), corresponding to the 6-fold modulation of the hexagonal pattern of grid cells, characterized by a 60° periodicity. In contrast, no significant clusters were detected corresponding to either 5-fold (72° periodicity) or 7-fold (51.4° periodicity) modulation. An additional ROI analysis with an anatomical ERC mask corroborated the robustness of the 6-fold modulation (Fig.1f, $t(9) = 3.89$, $p = 0.003$; Cohen's $d = 1.2$), not the 5- or 7-fold modulations (Fig.1f, 5-round: $t(9) < 1$, 7-round: $t(9) < 1$). These results confirmed the involvement of entorhinal grid cells in the object space where the object-matching task occurred, consistent with previous findings (e.g., Doeller et al., 2010, Constantinescu et al., 2016; Bao et al., 2019; Wagner et al., 2023; Raithel et al., 2023).

Anatomically, the HPC receives afferent projections from the ERC (Witter & Amaral, 1991; van Groen et al., 2003; Garcia and Buffalo, 2020), suggesting a potential for observing periodical neural activity patterns in the HPC because of the neural periodicity in the ERC. To test this intuition, our experimental design mandated that participants explored the full range of conceptual directions, ranged from 0° to 360° in increments of 1°, allowing the examination of hippocampal spatial periodicities of neural activities in addition to the established 60° periodicity. Specifically, we employed spectral analysis (see Methods for detail), which obviates the need for the prior hypothesis on periodicities or phase-offset calibrations as necessitated by the sinusoid analysis (Doeller et al., 2010; Constantinescu et al., 2016; Bao et al., 2019; Wagner et al., 2023; Raithel et al., 2023), to explore periodicity spectrum within the medial temporal lobe (MTL). In this analysis, conceptual directions were down-sampled into 15° bins, generating a vector of resampled directions (e.g., 0°, 15°, and 30°), thereby enabling the detection of frequencies up to 11 Hz. A Fast Discrete Fourier Transform (FFT) was performed on the direction-dependent activity series, as estimated by GLM and sorted in ascending order (Fig.2a). Spectral power was then extracted for each voxel, ranging from 0 Hz to 11 Hz. As a result, we observed a significant cluster with an

FFT magnitude centered at 3 Hz within the anterior portion of the right HPC (Fig.2b; $p < 0.05$, initial threshold; $p < 0.05$, SVC for multiple comparisons; Cohen's $d = 0.9$). Visual inspection further indicated that this peak magnitude at 3 Hz was presented in the CA1 region of the HPC. Additionally, the direction-dependent activity series, extracted via an anatomical mask of the anterior HPC, showed a discernible 3-fold periodic neural activity pattern that fluctuates as a function of conceptual directions (Fig.2c & d). The 3-fold modulation in the HPC was not due to the down-sampling of directions into 15° bins, as this finding was reliably observed when using both 10° and 20° bins (Fig. S4). Taken together, our spectral analysis successfully identified a robust 3-fold periodicity located in the CA1 region of the HPC.

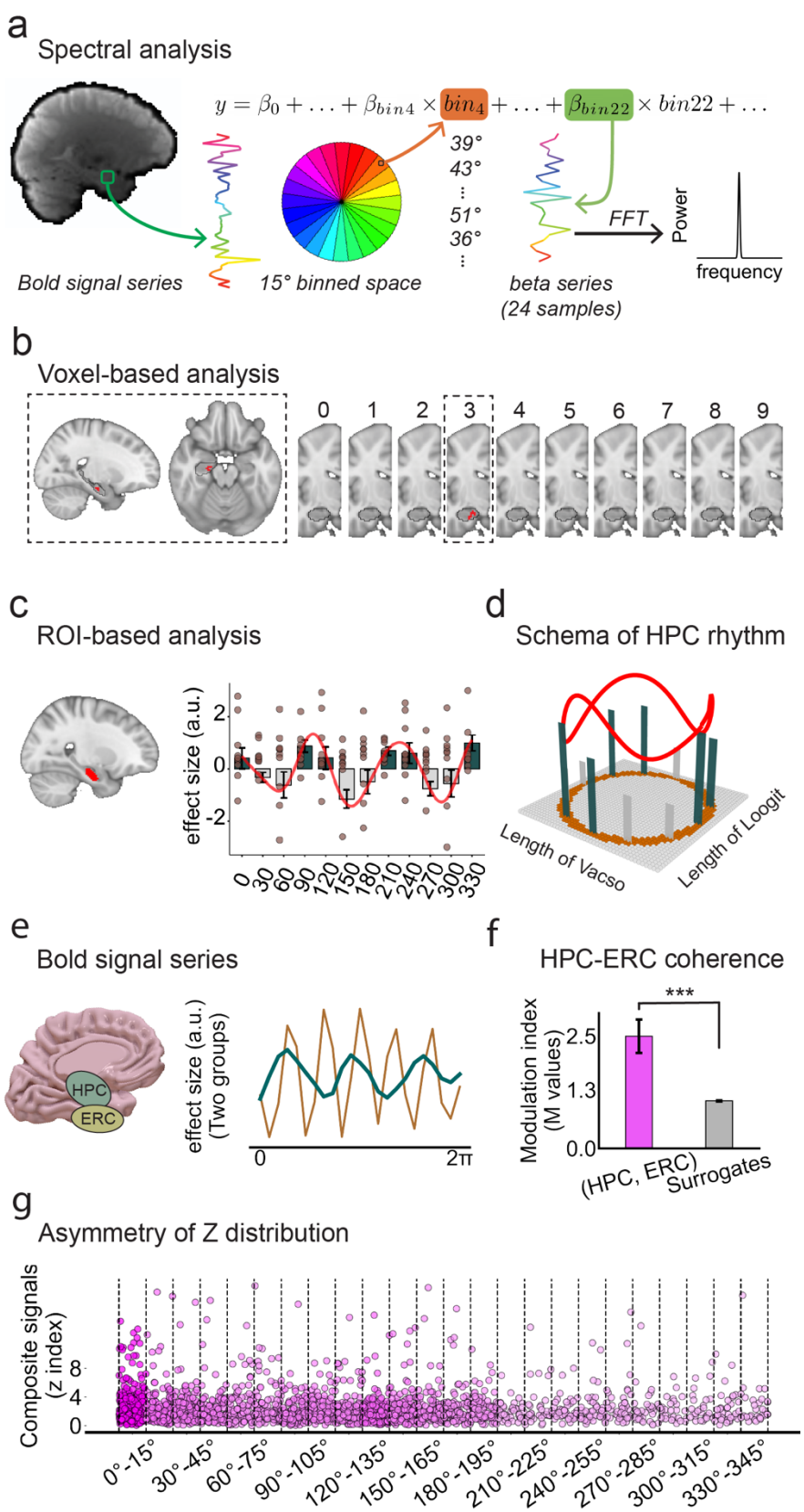
a
Spectral analysis
$y = \beta_0 + \ldots + \beta_{bin4} \times bin_4 + \ldots + \beta_{bin22} \times bin22 + \ldots$
39°
43°
51°
36°
FFT
Power
frequency
Bold signal series
15° binned space
beta series
(24 samples)
b
Voxel-based analysis
0 1 2 3 4 5 6 7 8 9
c
ROI-based analysis
effect size (a.u.)
2
0
-2
0 30 60 90 120 150 180 210 240 270 300 330
d
Schema of HPC rhythm
Length of Vacso
Length of Loogit
e
Bold signal series
HPC
ERC
effect size (a.u.)
(Two groups)
0
2π
f
HPC-ERC coherence
***
Modulation index
(M values)
2.5
1.3
0.0
(HPC, ERC)
Surrogates
g
Asymmetry of Z distribution
Composite signals
(z index)
8
4
0
0°-15°
30°-45°
60°-75°
90°-105°
120°-135°
150°-165°
180°-195°
210°-225°
240°-255°
270°-285°
300°-315°
330°-345°

Figure 2. Three-fold modulation in the HPC and its synchronization with 6-fold modulation in the ERC. a) Schema illustrating the procedure of spectral analysis to identify neural periodicities within the MTL. b) Voxel-based spectral analysis revealed a significant 3-fold modulation in the right HPC (Peak MNI coordinate: 20, -14, -18). c) The 3-fold modulation of the HPC based on the anatomical mask of bilateral HPC. d) Three-dimensional schema illustrating the relationship between the 3-fold modulation in the HPC and conceptual directions within the object space. e) Visual inspection on the averaged BOLD signal series, extracted from anatomical masks of the HPC (green) and the ERC (yellow), showed a phase-locked pattern. f-g) Amplitude-phase coupling analysis on the ERC and HPC activity series corroborated the significant coherence of HPC and ERC activity series, suggested by f) the significantly higher modulation index M (purple) as compared to that of surrogates (gray) and g) the asymmetric distribution of composite z values as a function of movement directions. Note that the probability density (denoted by the color scale of purple) showed the strongest density (darker purple) at the 0°-15° bin, consistent with the observation of the phase shift. Error bars indicate SEM. ***: $p < 0.001$

The hippocampal 3-fold modulation has not been previously reported in the spatial domain either by neurophysiological or fMRI studies. To validate the reliability of this finding, we therefore recruited a completely new group of participants (i.e., the replication group) and conducted the experiment at a different imaging center. The experimental design, data preprocessing and analyses remained identical with the original experimental group. In short, we replicated all major findings reported earlier (Fig.S5). That is, we found the involvement of grid cells in the right ERC (Fig.S5a, $p < 0.01$, initial threshold; $p < 0.05$, SVC for multiple comparison; Cohen's $d = 0.7$), and also identified the 3-fold modulation in the CA1 region of the right HPC (Fig.S5b, $p < 0.05$, initial threshold; $p < 0.05$, SVC for multiple comparison; Cohen's $d = 3.3$). The results in the replication study substantiate the reliability of the 3-fold modulation observed in the HPC.

To further explore the notion that the observed periodic neural activity in the HPC may originate from the periodic activity of grid cells in the ERC, we investigated whether the phases of these two periodic activities were synchronized. To do this, we extracted the BOLD signal series from each of the ERC and HPC of each participant, using data derived from the sinusoid and spectral analyses, respectively. Visual inspection shows that 80% of the participants exhibited discernible

phase-locked patterns (Fig.S6), characterized by the overlapping peaks of 3-fold and 6-fold periodicities (Fig.2e). To corroborate the observation, an amplitude-phase modulation analysis was employed to quantify the extent of cross-frequency coherence between the ERC and HPC. Specifically, the amplitude envelope from high-frequency activity series in the ERC and the phase of low-frequency activity series in the HPC were extracted. The composite signal z was constructed at each sample point through $z = A_{ERC}e^{i\phi_{HPC}}$ (Canolty et al., 2006). The modulation index M was derived by computing the mean of vector Z for the composite signal series and permutated surrogates of each participant. This analysis revealed a significantly higher modulation strength relative to surrogate controls (Fig. 2f; $t(19)=3.77$, $p<0.001$), suggesting a phase coherence between the ERC and HPC. Moreover, the radial asymmetry, observed from the probability density function of Z indices, signifies the presence of shared mutual information encoded in specific phases (i.e., movement directions) between the ERC and HPC (Fig.2g). Notably, the highest density of Z indices was found within the 0°-15° bin ($p < 0.05$, corrected for multiple comparisons), fitting nicely with the observed phase shift shown in Fig. 2e. Taken together, both visual inspection and statistical analyses indicated that peaks in the ERC activity series selectively aligned with those in the HPC activity. Note that this result differs from prior work in the temporal domain, where neural activity coherence is typically characterized by the modulation of low-frequency bands on high-frequency signals (e.g., Buzsaki, 2006; Maris et al., 2011; Friese et al., 2013). Rather, our results suggest a potential causal link between the formation of 3-fold periodicity of hippocampal place cells and the 6-fold periodicity of entorhinal grid cells, despite pronounced individual differences in the phase of activity series across participants (Fig.S6).

The "E-H PhaseSync" Model

To demonstrate the mechanism of hippocampal 3-fold periodicity and its role in the vector field formation, we built a hypothetical model termed as the "E-H PhaseSync" model, hypothesizing that the entorhinal projections form the 3-fold periodicity of the HPC via the ERC-HPC circuit (Fyhn et al., 2007; Hales et al., 2014). Then, the 3-fold modulation serves as the periodic scaffold embedding movement directions (McNaughton et al., 1983; Muller et al., 1994; Rubin et al., 2014; Meister and Buffalo, 2016) and vectorial fields (Leutgeb et al., 2000; Sarel et al., 2017; Ormond and O'Keefe., 2022) in the HPC. These intuitions are supported by three neuroscience evidences. First, the grid orientation and spacing are almost invariant (Hafting et al., 2005; Stensola et al.,

2015; Krupic et al., 2015; Gardner et al., 2022), the downstream area that receives the grid codes activated by mental imagination (Hasselmo, 2009; Buckner, 2010; Mullally and Maguire, 2014; Lisman et al., 2017; Whittington et al., 2022) may fluctuate as a function of spatial orientations due to the three primary axes of hexagonal pattern. Second, the vector trace cells (VTCs) in the subiculum showed trace fields in representing location sequence (Tsao et al., 2013; Bicanski and Burgess, 2018; Bicanski and Burgess, 2020; Poulter et al., 2021), which might be projected from grid cell populations (Naber et al., 2001) and were sending into the CA1 of the HPC (Sun et al., 2019). Third, the grid cell activity structured by spatial orientations can be stably elicited by movement directions (Doeller et al., 2010; Constantinescu et al., 2016; Nau et al., 2018; Bao et al., 2019; Wagner et al., 2023), reflecting that spatial orientation might be the basis of direction formation.

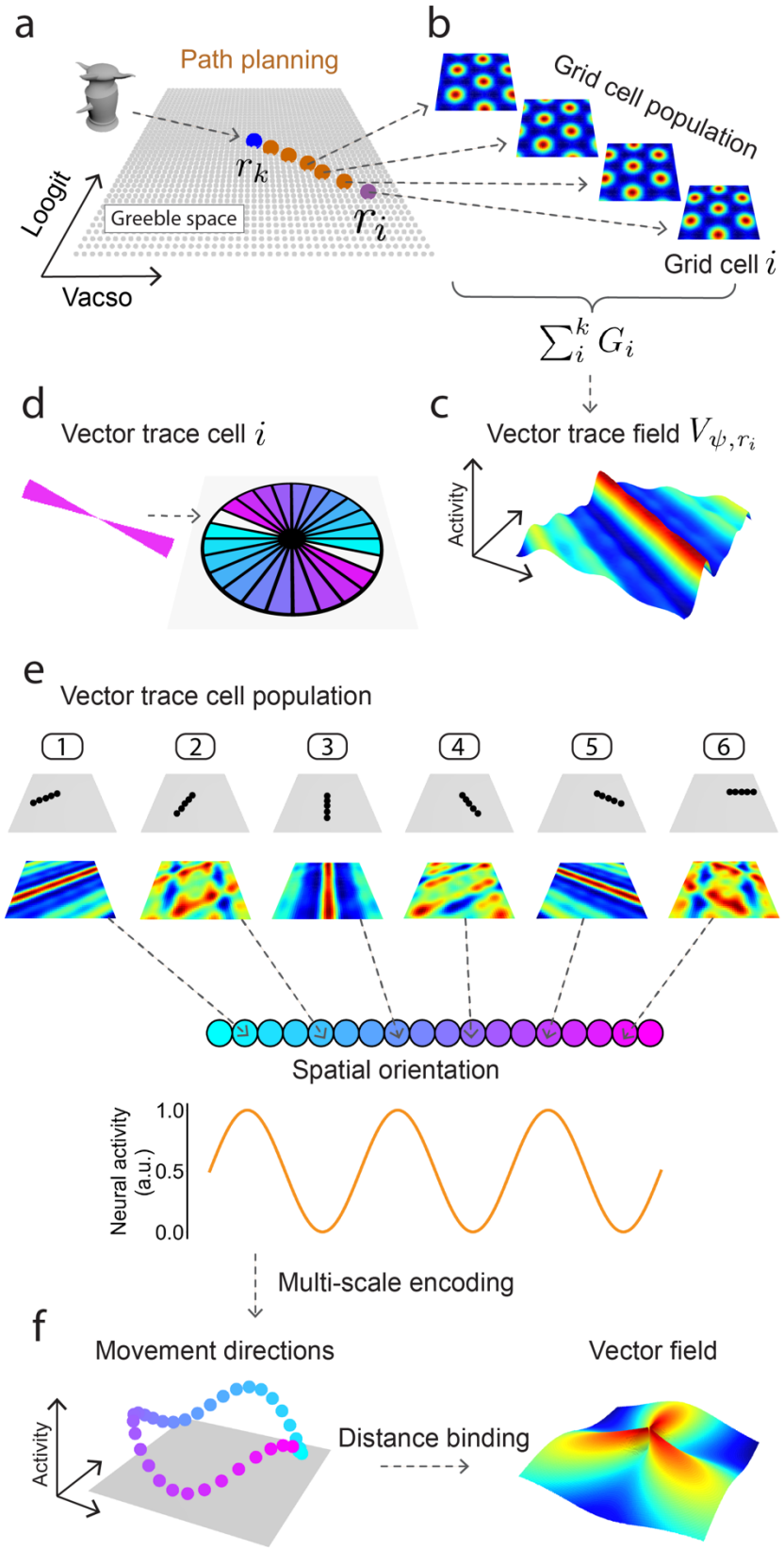
a
Path planning
Loogit
Greeble space
Vacso
b
Grid cell population
Grid cell i
$\sum_i^k G_i$
d
Vector trace cell i
c
Vector trace field V_{ψ,r_i}
Activity
e
Vector trace cell population
1
2
3
4
5
6
Spatial orientation
Neural activity (a.u.)
1.0
0.5
0.0
Multi-scale encoding
f
Movement directions
Vector field
Activity
Distance binding

Figure 3. The hypothetical E-H PhaseSync Model for the formation of hippocampal vector field. a) the path planning originated from the self-location r_i (purple dot) to the goal-location r_k (blue dot) on the object space throughout imagination (orange dots). b) the entorhinal grid cells activated during path planning. Those grid cells were generated in advance for each location of the object space. c) the response field V_{ψ,r_i} of vector trace cell, which has been known in the subiculum and encodes the spatial orientation ψ at location r_i, was generated by conjunctive grid codes. d) schema of the spatial representation of single vector trace cell, which indicates the spatial orientation that is independent to self-location (i.e., a single neuron symmetrically encodes the movement direction i and the direction i+180°). The color scale denotes the spatial orientations ranged from 0° to 180° that tessellate the object space. e) the three-fold modulation of vector trace cell population. The 2D representation of paths were transformed to a scalar value δ_r throughout the winner-take-all dynamics, which evaluates to what extend the spatial orientation ψ_r differs from the movement direction ϕ'_r (i.e., ϕ_r mod 180°) pointing to goal. The activated vector trace cell corresponds to a smaller δ_r, indicating the optimized orientation for upcoming action. The vector of δ_r forms the three-fold scaffold with the peaks denoting the three orientations (i.e., ①③⑤) that align to the primary axes of grid cell. The color scale denotes the spatial orientations ranged from 0° to 180°. f) the activity of CA1 neurons was aligned by the three-fold scaffold of the subiculum throughout multi-scale encoding, resulting in the direction map $C_{Direction}$, which finally forms the vector field map C by integrating distance $C_{Location}$. The color scale in the dot plot denotes the movement directions ranged from 0° to 360°.

The E-H PhaseSync model simulated path integration from each starting location r on the object space throughout mental imagination (Fig.3a), which is also known as "forward replay" (Diba and Buzsáki, 2007; Dragoi and Tonegawa, 2011; Pfeiffer, 2020), where the receptive field of neuron r_i activates a sequence of spatially adjacent neurons along the spatial orientation ψ (Fig.3b). The conjunctive representation $V_{\psi,r}$ of activated neurons exhibited the planar wave (Fig.3c), the pattern previously found in the medial ERC of freely moving rats (Welday et al., 2011, Krupic et al., 2012), if the current orientation ψ aligns to the movement direction φ that points to the goal.

Since the symmetry of the object space, each $V_{\psi,r}$ encodes a unique spatial orientation, which was extracted by the VTC population. Each VTC cell was characterized by two parameters. One is the orientation selectivity ψ, which was computed by the maxima of the vector Ψ (Equation 1), indicating the symmetrical encoding of movement direction i and i + 180° (i.e., $\psi = i$). In other words, the object space can be tessellated by the trace fields ranged from 0° to 180° (Fig.3d). The second parameter is the activity strength δ, indexed by how close the preferred orientation aligns to the correct movement direction (Equation 5 & 6). Therefore, the VTC population encodes a three-fold scaffold, which embeds preferred orientations with each indexed by activity strength δ (Fig.3e).

$$\Psi = \{\sum_i^k V_{\psi,r_i}\}_{\psi=0}^{\pi} \tag{1}$$

The vector field C of the HPC was generated by the linear summation of the spatial representation of movement direction $C_{Direction}$ and the spatial representation of distance $C_{Location}$ (Equation 2). $C_{Location}$ was simulated by a Q-value map after training a RL model (see methods for details).

$$C = C_{\text{Direction}} + C_{\text{Location}} \tag{2}$$

$C_{Direction}$, illustrated by the cosine function in Equation 3, inherited the spatial frequency f_δ and the phase θ_δ of VTC population (Fig.3f), which fluctuated as a function of spatial orientations. The term $\arctan\left(\frac{r'_y}{r'_x}\right)$ denotes the movement directions determined by the location shifts r'_x and

r'_y relative to goal-location, which complies with the hippocampal multi-scale encoding (Poppenk et al., 2013; Collin et al., 2015; Robinson et al., 2015; Brunec et al., 2018), the fine-grained representation of movement directions required more place cells relative to the coarse representation. Accordingly, the increased number of neurons was accompanied with the spatial phase precession (Fig.S7), consistent with a recent discovery (Qasim et al., 2021).

$$\mathrm{C}_{\mathrm{Direction}r} = \cos(f_\delta \arctan(\frac{r'_y}{r'_x}) + \theta_\delta) \tag{3}$$

Finally, the vector field C provides a navigational vector from the current location of agent towards to goal. During path integration, the movement transition referred to the strongest activity of C_r surrounding to self-location.

Three-fold modulation in behavior performance

During the implementation of E-H PhaseSync Model, the model performed path integration for each trial throughout continuously accepting agent's location as input and outputting the next location until the goal was reached, a total of 156 trials were completed. As the result, agent's trajectories exhibited the anisotropic three-fold pattern modulated by the movement directions (Fig.4a). To quantify the result, we computed the traveling length of each trial by summing the distances of all location-pairs in the trial. The result showed the three-fold fluctuation of traveling length across the movement directions ranged from 0° to 360° (Fig.4b). Spectral analysis further confirmed the significant three-fold periodicity (Fig.4c, red arrow; $p < 0.05$, corrected for multiple comparisons), while no significant spectral power was found for other periodic modulations (Fig.4c). Contrary to the commonly held assumption of an isotropic performance in movement directions, our results suggested that agent's performance will be influenced by grid orientations. The start-location oriented by the spatial orientation aligning to grid axes tends to a higher performance than the start-location oriented by the orientation misaligning to grid axes.

Model prediction

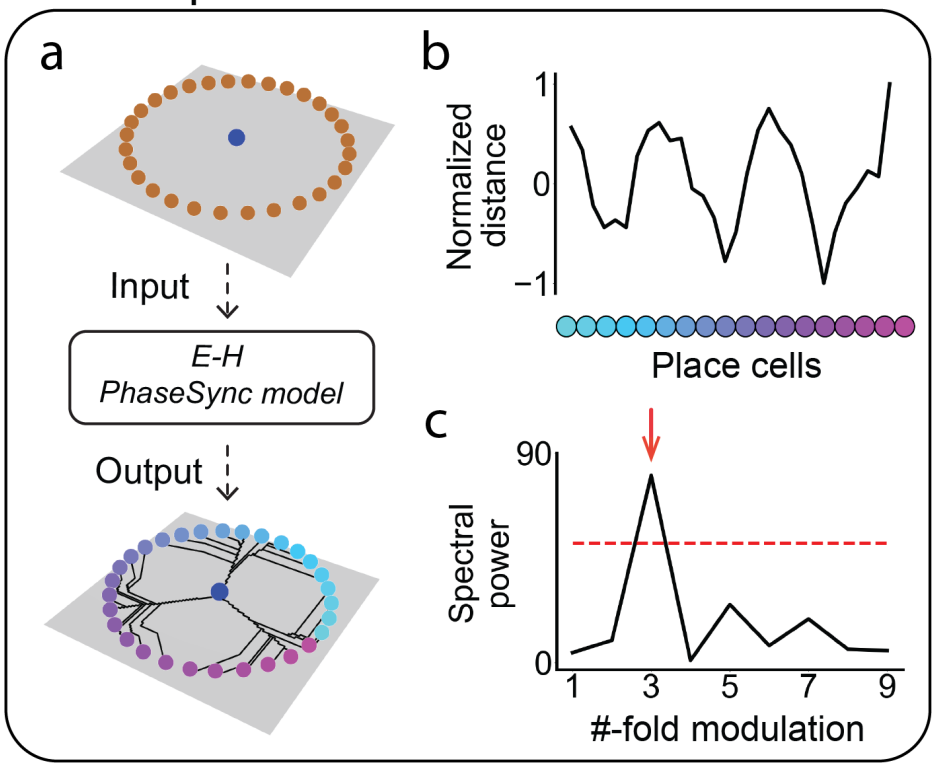

Human behavior

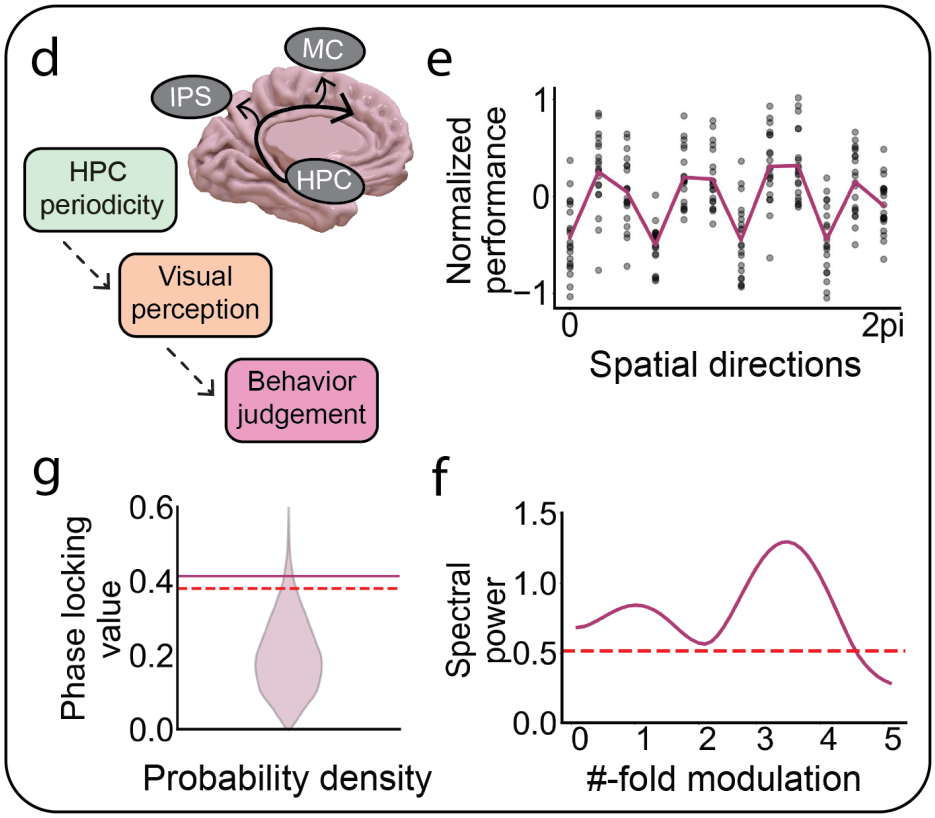

Figure 4. Three-fold periodicity of model and human performance. a) the implementation of E-H PhaseSync model, which receives each of the starting locations arranged in a ring-shaped pattern as input and outputs the upcoming locations reaching the goal. Thirty starting-locations were used for illustration purpose. b) model performance, measured by the normalized traveling length, fluctuated as a function of movement directions. Note that the traveling length would be shorter if movement direction aligns with the primary axis of grid cell. c) the three-fold modulation of model performance revealed by spectral analysis. The red dashed line indicates the baseline derived from permutation. The arrow denotes the peak of power spectrum. d) the visuomotor circuit of brain that may inherits the 3-fold effect of the HPC. IPS: Intra Parietal Sulcus; MC: Motor Cortex. e) human performance fluctuated as a function of movement directions. The performance of each direction was measured by the composite index of the path length and the deviation between the goal and stop location. f) the significant spectral power of human performance was found at the frequency of 3.36 Hz. The red dashed line denotes the baseline derived from permutation. g) Phase-phase coherence between human performance and hippocampal BOLD signal series. The Phase-Lock Value (PLV, purple line) exceeded the threshold of the 95th percentile of PLV distribution obtained from randomly shuffled surrogates (red dashed line).

We next questioned whether the three-fold periodicity have emerged in the behavioral performance of human participants. In addition to the prediction of E-H PhaseSync Model, this hypothesis is supported by brain's visual-motor system, where the hippocampal periodic activity may propagates to the egocentric areas such as the precuneus and the lateral parietal cortex, hereby modulating the performance of visuospatial decision (Fig. 4d). To examine the hypothesis, we quantified the behavioral performance of human participant by two factors. One was the traveling length, another was the deviation between the goal location and the final endpoint (i.e., error size, see method for details). Both shorter traveling length and smaller error magnitude indicate better performance. As the result, the averaged performance of human participant was clearly fluctuated as a function of movement directions in approximate 3-fold modulation (Fig. 4e). The behavioral periodicity could be even observable at individual level, 16 out of 20 participants exhibited the 3-fold periodicity in task performance (Fig.S8). Spectral analysis confirmed the significance of human's three-fold behavioral periodicity by identifying the peak of spectral power at 3.36-fold (Fig. 4f; $p < 0.05$, corrected for multiple comparisons). Next, to further examine the causal

relationship between the hippocampal periodicity and behavioral periodicity, we computed the phase-locking coherence across human participants, and the result suggested significant Phase-Locking Value (PLV) that was higher than the shuffled control (Fig.4g; $p < 0.05$, corrected for multiple comparisons), confirming the influence of the hippocampal periodicity on behavioral periodicity. Taken together, these results demonstrated that the performance periodicity of human participants corroborated the model prediction, thereby substantiating the model as a mechanistic framework the vector field formation in the HPC.

Discussion

Path integration, denoting the ability in accessing spatial knowledge from the last moment of updating to the current one in both physical (Wang and Spelke; Gallistel, 2017) and abstract space (Epstein et al., 2017; Behrens et al., 2018; Park et al., 2020), is realized especially by the HPC and ERC of the hippocampal complex. However, the two regions perform distinct functions: entorhinal grid cells essentially create coordinate system, which encodes continuous space in discrete manner (Hafting et al., 2005), while the firing field of hippocampal place cells offers the localized representation of space (O'Keefe & Dostrovsky, 1971). With both empirical experiments and computational modeling, we investigated how the two regions work as whole to achieve path integration. Owe to the large scope of fMRI scanning, we discovered spatial neural periodicity of 3-fold modulation in the CA1 area of HPC that signifies the existence of hippocampal vector fields necessary for path integration. Critically, the periodicity's phase was locked to that of the established spatial periodicity of 6-fold modulation in the ERC. Based on the intuition of the hippocampal periodicity resulted from the projection of entorhinal grid cells, our E-H PhaseSync Model showed how the vector fields can be formed throughout constructing the three-fold scaffold of spatial orientations to represent movement directions from populational grid codes, which in turn integrated distance for path integration. Our results provided a mechanistic explanation to the neural periodicity of the ERC-HPC circuit during path integration.

The present E-H PhaseSync Model has built a bridge to connect the possible principles of how brain encodes spatial metric, spatial orientation, and movement direction. These pieces of spatial information may be structured by independent cognitive maps, ranging from the abstract (i.e.,

spatial metric) to the actual (i.e., movement direction) dimension. The hypothesized representation of spatial orientation generated by the conjunctive grid codes via mental imagination not only explained multiple previously hypothesized periodic representations in the brain such as the planar waves proposed by "grid cell to place cell" model (Solstad et al., 2006; de Almeida et al., 2009; Bush et al., 2014; Bush et al., 2015; Bicanski and Burgess, 2019), the oscillatory interference (Welday et al., 2011), and the spatially periodic bands (Krupic et al., 2012), but also supported the recent discovered vector trace cells in the subiculum (Tsao et al., 2013; Bicanski & Burgess, 2018; Bicanski & Burgess, 2020; Poulter et al., 2021), where the trace fields can be irregular (Tsao et al., 2013; Poulter et al., 2021), corresponding to an explanation of the misalignment between grid orientation and movement direction. In addition, the hypothesized representation of spatial orientation also well explained the discovery from the reorientation studies (Hermer & Spelke, 1994; Julian et al., 2015; Julian et al., 2018). Rodents and young children often use nongeometric features for place recognition, leading to equally searching at the rewarded and geometrically equivalent opposite, and simultaneously failed to use nongeometric features for heading retrieval. This phenomenon has been explained by the existence of separate systems for place recognition and heading retrieval. Our results supported this viewpoint, the geometric cue in these studies might corresponds to spatial orientation, which failed to bind the nongeometric cues encoded in the HPC to perceive the heading direction.

The navigational models (Banino et al., 2018; Gao et al., 2018; Bicanski & Burgess, 2019; Whittington et al., 2020; Edvardsen et al., 2020), as well as the present E-H PhaseSync Model, have been heavily relying on the simulation of the hippocampal and entorhinal neurons. However, the computational principle of these neurons was not fully understood. Our results supported the periodic computation, which embeds spatial orientations and movement directions into the periodic scaffold defined by spatial phases and spatial frequency. Together with the spatial selectivity of neurons, possibly first discussed by Hubel and Wiesel (1959; 1962) regarding the visual location representation of ganglion cells, and the phase-coupled behavioral periodicity with the hippocampal activity revealed in the present study, the periodic scaffold might play a general principle to structure the information in both spatial and temporal domain omnipresent in the brain, particularly the brain areas beyond the MTL (see also Bieri et al., 2014; Fiebelkorn et al., 2018; Staudigl et al., 2018). Therefore, the metric of grid hexagonal pattern is apparently not the only

source of the formation of the hippocampal vector fields, as the hippocampus also receives external visual cues that provide local geometry especially when allocentric map is not accessible (Gallistel, 2017; Julian et al., 2018; Keinath et al., 2017). Therefore, even before stable grid cell activity is present (Wills et. al., 2010; Langston et al., 2010) or by silencing grid cells (Koenig et al (2011), the place codes of location are little affected and the freely forage in open fields is apparently normal. Future studies are thus invited to explore spatial periodic coding in the entire brain, which may help understanding how information is organized, stored, and retrieved.

According to the empirical evidence of the three-fold periodicity of the HPC, we have proposed the E-H PhaseSync Model to explain how the three-fold periodicity was probably generated within the ERC-HPC circuit, and how it supported the direction encoding of place cells (McNaughton et al., 1983; Muller et al., 1994; Leutgeb et al., 2000; Rubin et al., 2014; Meister and Buffalo, 2016; Sarel et al., 2017; Ormond and O'Keefe., 2022). However, one limitation of our study is that we do not provide enough biological evidences to support the model. Future studies may particularly focus on the neural representation of spatial orientation and the neural representation of periodic scaffold that embedding the movement directions. Another limitation of this study is that the E-H PhaseSync model does not illustrate the formation of hippocampal vector field within a context-specific scene during learning. For example, how the vector fields are updated by unexpected landmark or obstacle impact? One possibility is that the ERC receives the context and identity of updated goal (e.g., an intermediate landmark) from the parahippocampal cortex and perirhinal cortex (Eichenbaum and Lipton, 2008; Montaldi and Mayes, 2010; Wilson et al., 2013), and anchors the intermediate goal locations into environmental metric (Stensola et al., 2015; Bottini and Doeller, 2020) through the excitation-inhibition dynamics of neurons (Amari, 1977; Samsonovich & McNaughton, 1997; Fuhs & Touretzky, 2006; Burak & Fiete, 2009; Couey et al., 2013). Taken together, further work may need to build the periodicity-based model to simulate the navigational process of brain (Rennó-Costa and Tort, 2017; Whittington et al., 2020), the interactive principle among a variety of cognitive maps that flexibly organized by ongoing experiences would greatly help to explain the unified percept of the world efficiently (VanRullen and Kanai, 2021).

Data availability

The data that support the findings of the present study are available from the corresponding author (J.L.) upon request.

Code availability

All analyzes reported in the present study were conducted with the customized codes written in Python (version 3.9), Pygame (version 2.0), Matlab (version 2019b), R (version 4.0), and GNU bash (version 3.2.57). The codes will be available from the corresponding author (J.L.) upon request. The neuroimaging toolbox and machine learning framework used by the present work are publicly available as following: FreeSurfer (v7.1, https://surfer.nmr.mgh.harvard.edu/), FSL (version 6.0, https://fsl.fmrib.ox.ac.uk/fsl/fslwiki;), and Torch (version 1.9, https://pytorch.org/).

Acknowledgments

We gratefully acknowledge Mr. Yue Wu and Ms. Yuannan Li for helpful discussions during data analysis, Prof. Russell Epstein for valuable comments on the results of fMRI and computational modelling, and Dr. Michael Tarr for sharing the code for greeble stimulus generation. Computational work was supported by High-performance Computing Platform of Peking University. The work was supported by the National Key R&D Program of China (2020AAA0105200), China Postdoctoral Science Foundation (2022M710470), Beijing Municipal Science & Technology Commission & Administrative Commission of Zhongguancun Science Park (Z221100002722012), Tsinghua University Guoqiang Institute (2020GQG1016), and Beijing Academy of Artificial Intelligence (BAAI).

Conflict of interest

None declared

Author Contributions

J.L. conceived the study and provided advice. B.Z. conducted the fMRI study, performed the analysis, and built the computational model. B.Z. and J.L. wrote the paper.

Reference

Amari, S. (1977). Dynamics of pattern formation in lateral-inhibition type neural fields. Biol Cybern, 27(2), 77-87. https://doi.org/10.1007/BF00337259

Buzsaki, G. (2006). *Rhythms of the Brain*. Oxford university press.

Burgess, N., Barry, C., & O'Keefe, J. (2007). An oscillatory interference model of grid cell firing. Hippocampus, 17(9), 801-812. https://doi.org/10.1002/hipo.20327

Blair, H. T., Welday, A. C., & Zhang, K. (2007). Scale-invariant memory representations emerge from moire interference between grid fields that produce theta oscillations: a computational model. Journal of Neuroscience, 27(12), 3211-3229.

Burak, Y., & Fiete, I. R. (2009). Accurate path integration in continuous attractor network models of grid cells. PLoS Comput Biol, 5(2), e1000291. https://doi.org/10.1371/journal.pcbi.1000291

Buckner, R. L. (2010). The role of the hippocampus in prediction and imagination. *Annual review of psychology*, *61*, 27-48.

Bush, D., Barry, C., & Burgess, N. (2014). What do grid cells contribute to place cell firing? Trends Neurosci, 37(3), 136-145. https://doi.org/10.1016/j.tins.2013.12.003

Bieri, K. W., Bobbitt, K. N., & Colgin, L. L. (2014). Slow and fast gamma rhythms coordinate different spatial coding modes in hippocampal place cells. Neuron, 82(3), 670-681. https://doi.org/10.1016/j.neuron.2014.03.013

Bush, D., Barry, C., Manson, D., & Burgess, N. (2015). Using grid cells for navigation. Neuron, 87(3), 507-520. https://doi.org/10.1016/j.neuron.2015.07.006

Behrens, T. E., Muller, T. H., Whittington, J. C., Mark, S., Baram, A. B., Stachenfeld, K. L., & Kurth-Nelson, Z. (2018). What is a cognitive map? Organizing knowledge for flexible behavior. Neuron, 100(2), 490-509.

Bicanski, A., & Burgess, N. (2018). A neural-level model of spatial memory and imagery. Elife, 7, e33752.

Banino, A., Barry, C., Uria, B., Blundell, C., Lillicrap, T., Mirowski, P., ... & Kumaran, D. (2018). Vector-based navigation using grid-like representations in artificial agents. Nature, 557(7705), 429-433.

Bush, D., & Schmidt-Hieber, C. (2018). Computational models of grid cell firing. Hippocampal Microcircuits: A Computational Modeler's Resource Book, 585-613.

Brunec, I. K., Bellana, B., Ozubko, J. D., Man, V., Robin, J., Liu, Z. X., ... & Moscovitch, M. (2018). Multiple scales of representation along the hippocampal anteroposterior axis in humans. Current biology, 28(13), 2129-2135.

Bicanski, A., & Burgess, N. (2019). A computational model of visual recognition memory via grid cells. Current Biology, 29(6), 979-990.

Bao, X., Gjorgieva, E., Shanahan, L. K., Howard, J. D., Kahnt, T., & Gottfried, J. A. (2019). Grid-like Neural Representations Support Olfactory Navigation of a Two-Dimensional Odor Space. Neuron, 102(5), 1066-1075 e1065. https://doi.org/10.1016/j.neuron.2019.03.034

Bicanski, A., & Burgess, N. (2020). Neuronal vector coding in spatial cognition. Nature Reviews Neuroscience, 21(9), 453-470.

Bottini, R., & Doeller, C. F. (2020). Knowledge across reference frames: Cognitive maps and image spaces. Trends in Cognitive Sciences, 24(8), 606-619.

Canolty, R. T., Edwards, E., Dalal, S. S., Soltani, M., Nagarajan, S. S., Kirsch, H. E., ... & Knight, R. T. (2006). High gamma power is phase-locked to theta oscillations in human neocortex. *science*, *313*(5793), 1626-1628.

Colgin, L. L., Moser, E. I., & Moser, M. B. (2008). Understanding memory through hippocampal remapping. *Trends in neurosciences*, *31*(9), 469-477.

Couey, J. J., Witoelar, A., Zhang, S. J., Zheng, K., Ye, J., Dunn, B., Czajkowski, R., Moser, M. B., Moser, E. I., Roudi, Y., & Witter, M. P. (2013). Recurrent inhibitory circuitry as a mechanism for grid formation. Nat Neurosci, 16(3), 318-324. https://doi.org/10.1038/nn.3310

Collin, S. H., Milivojevic, B., & Doeller, C. F. (2015). Memory hierarchies map onto the HPC's long axis in humans. Nature neuroscience, 18(11), 1562-1564.

Constantinescu, A. O., O'Reilly, J. X., & Behrens, T. E. J. (2016). Organizing conceptual knowledge in humans with a gridlike code. Science, 352(6292), 1464-1468. https://doi.org/10.1126/science.aaf0941

De Valois, R. L., Albrecht, D. G., & Thorell, L. G. (1982). Spatial frequency selectivity of cells in macaque visual cortex. Vision Res, 22(5), 545-559. https://doi.org/10.1016/0042-6989(82)90113-4

Diba, K., & Buzsáki, G. (2007). Forward and reverse hippocampal place-cell sequences during ripples. *Nature neuroscience*, *10*(10), 1241-1242.

Dehaene, S., & Cohen, L. (2007). Cultural recycling of cortical maps. Neuron, 56(2), 384-398. https://doi.org/10.1016/j.neuron.2007.10.004

De Almeida, L., Idiart, M., & Lisman, J. E. (2009). The input–output transformation of the hippocampal granule cells: from grid cells to place fields. *Journal of Neuroscience*, *29*(23), 7504-7512.

Doeller, C. F., Barry, C., & Burgess, N. (2010). Evidence for grid cells in a human memory network. Nature, 463(7281), 657-661. https://doi.org/10.1038/nature08704

Dragoi, G., & Tonegawa, S. (2011). Preplay of future place cell sequences by hippocampal cellular assemblies. *Nature*, *469*(7330), 397-401.

De Cothi, W., Nyberg, N., Griesbauer, E. M., Ghanamé, C., Zisch, F., Lefort, J. M., ... & Spiers, H. J. (2022). Predictive maps in rats and humans for spatial navigation. Current Biology, 32(17), 3676-3689.

Eichenbaum, H., & Lipton, P. A. (2008). Towards a functional organization of the medial temporal lobe memory system: role of the parahippocampal and medial entorhinal cortical areas. *Hippocampus*, *18*(12), 1314-1324.

Epstein, R. A., Patai, E. Z., Julian, J. B., & Spiers, H. J. (2017). The cognitive map in humans: spatial navigation and beyond. *Nature neuroscience*, *20*(11), 1504-1513.

Edvardsen, V., Bicanski, A., & Burgess, N. (2020). Navigating with grid and place cells in cluttered environments. Hippocampus, 30(3), 220-232.

Fyhn, M., Hafting, T., Treves, A., Moser, M. B., & Moser, E. I. (2007). Hippocampal remapping and grid realignment in entorhinal cortex. Nature, 446(7132), 190-194.

Friese, U., Köster, M., Hassler, U., Martens, U., Trujillo-Barreto, N., & Gruber, T. (2013). Successful memory encoding is associated with increased cross-frequency coupling between frontal theta and posterior gamma oscillations in human scalp-recorded EEG. Neuroimage, 66, 642-647.

Fiebelkorn, I. C., Pinsk, M. A., & Kastner, S. (2018). A Dynamic Interplay within the Frontoparietal Network Underlies Rhythmic Spatial Attention. Neuron, 99(4), 842-853 e848. https://doi.org/10.1016/j.neuron.2018.07.038

Fuhs, M. C., & Touretzky, D. S. (2006). A spin glass model of path integration in rat medial entorhinal cortex. Journal of Neuroscience, 26(16), 4266-4276.

Gauthier, I., & Tarr, M. J. (1997). Becoming a "Greeble" expert: exploring mechanisms for face recognition. Vision Res, 37(12), 1673-1682. https://doi.org/10.1016/s0042-6989(96)00286-6

Guanella, A., Kiper, D., & Verschure, P. (2007). A model of grid cells based on a twisted torus topology. Int J Neural Syst, 17(4), 231-240. https://doi.org/10.1142/S0129065707001093

Gallistel, C. R. (2017). Navigation: whence our sense of direction?. *Current Biology*, *27*(3), R108-R110.

Gao, R., Xie, J., Zhu, S. C., & Wu, Y. N. (2018). Learning Grid Cells as Vector Representation of Self-Position Coupled with Matrix Representation of Self-Motion. In International Conference on Learning Representations.

Gerlei, K., Passlack, J., Hawes, I., Vandrey, B., Stevens, H., Papastathopoulos, I., & Nolan, M. F. (2020). Grid cells are modulated by local head direction. Nature communications, 11(1), 4228.

Garcia, A. D., & Buffalo, E. A. (2020). Anatomy and function of the primate entorhinal cortex. *Annual Review of Vision Science*, *6*, 411-432.

Gardner, R. J., Hermansen, E., Pachitariu, M., Burak, Y., Baas, N. A., Dunn, B. A., ... & Moser, E. I. (2022). Toroidal topology of population activity in grid cells. *Nature*, *602*(7895), 123-128.

Hubel, D. H., & Wiesel, T. N. (1959). Receptive fields of single neurones in the cat's striate cortex. J Physiol, 148, 574-591. https://doi.org/10.1113/jphysiol.1959.sp006308

Hubel, D. H., & Wiesel, T. N. (1962). Receptive fields, binocular interaction and functional architecture in the cat's visual cortex. J Physiol, 160, 106-154. https://doi.org/10.1113/jphysiol.1962.sp006837

Hermer, L., & Spelke, E. S. (1994). A geometric process for spatial reorientation in young children. Nature, 370(6484), 57-59.

Hafting, T., Fyhn, M., Molden, S., Moser, M. B., & Moser, E. I. (2005). Microstructure of a spatial map in the entorhinal cortex. Nature, 436(7052), 801-806. https://doi.org/10.1038/nature03721

Hasselmo, M. E. (2009). A model of episodic memory: mental time travel along encoded trajectories using grid cells. Neurobiology of learning and memory, 92(4), 559-573.

Hales, J. B., Schlesiger, M. I., Leutgeb, J. K., Squire, L. R., Leutgeb, S., & Clark, R. E. (2014). Medial entorhinal cortex lesions only partially disrupt hippocampal place cells and hippocampus-dependent place memory. Cell reports, 9(3), 893-901.

Insausti, R., Juottonen, K., Soininen, H., Insausti, A. M., Partanen, K., Vainio, P., Laakso, M. P., & Pitkanen, A. (1998). MR volumetric analysis of the human entorhinal, perirhinal, and temporopolar cortices. AJNR Am J Neuroradiol, 19(4), 659-671. https://www.ncbi.nlm.nih.gov/pubmed/9576651

Iglesias, J. E., Augustinack, J. C., Nguyen, K., Player, C. M., Player, A., Wright, M., Roy, N., Frosch, M. P., McKee, A. C., Wald, L. L., Fischl, B., Van Leemput, K., & Alzheimer's Disease Neuroimaging, I. (2015). A computational atlas of the hippocampal formation using ex vivo, ultra-high resolution MRI: Application to adaptive segmentation of in vivo MRI. Neuroimage, 115, 117-137. https://doi.org/10.1016/j.neuroimage.2015.04.042

Jenkinson, M., & Smith, S. (2001). A global optimisation method for robust affine registration of brain images. Med Image Anal, 5(2), 143-156. https://doi.org/10.1016/s1361-8415(01)00036-6

Johnson, A., Seeland, K., & Redish, A. D. (2005). Reconstruction of the postsubiculum head direction signal from neural ensembles. Hippocampus, 15(1), 86-96.

Jeffery, K. J. (2007). Integration of the sensory inputs to place cells: what, where, why, and how?. *Hippocampus*, *17*(9), 775-785.

Julian, J. B., Keinath, A. T., Muzzio, I. A., & Epstein, R. A. (2015). Place recognition and heading retrieval are mediated by dissociable cognitive systems in mice. Proceedings of the National Academy of Sciences, 112(20), 6503-6508.

Jeffery, K. J., Page, H. J., & Stringer, S. M. (2016). Optimal cue combination and landmark-stability learning in the head direction system. The Journal *of physiology*, *594*(22), 6527-6534.

Julian, J. B., Keinath, A. T., Marchette, S. A., & Epstein, R. A. (2018). The neurocognitive basis of spatial reorientation. *Current Biology*, *28*(17), R1059-R1073.

Koenig, J., Linder, A. N., Leutgeb, J. K., & Leutgeb, S. (2011). The spatial periodicity of grid cells is not sustained during reduced theta oscillations. *Science*, *332*(6029), 592-595.

Krupic, J., Burgess, N., & O'Keefe, J. (2012). Neural representations of location composed of spatially periodic bands. Science, 337(6096), 853-857. https://doi.org/10.1126/science.1222403

Killian, N. J., Jutras, M. J., & Buffalo, E. A. (2012). A map of visual space in the primate entorhinal cortex. Nature, 491(7426), 761-764. https://doi.org/10.1038/nature11587

Krupic, J., Bauza, M., Burton, S., Barry, C., & O'Keefe, J. (2015). Grid cell symmetry is shaped by environmental geometry. *Nature*, *518*(7538), 232-235.

Keinath, A. T., Julian, J. B., Epstein, R. A., & Muzzio, I. A. (2017). Environmental geometry aligns the hippocampal map during spatial reorientation. *Current Biology*, *27*(3), 309-317.

Kang, L., & Balasubramanian, V. (2019). A geometric attractor mechanism for self-organization of entorhinal grid modules. Elife, 8, e46687.

Landau, A. N., & Fries, P. (2012). Attention samples stimuli rhythmically. Curr Biol, 22(11), 1000-1004. https://doi.org/10.1016/j.cub.2012.03.054

Leutgeb, S., Ragozzino, K. E., & Mizumori, S. J. (2000). Convergence of head direction and place information in the CA1 region of hippocampus. Neuroscience, 100(1), 11-19.

Langston, R. F., Ainge, J. A., Couey, J. J., Canto, C. B., Bjerknes, T. L., Witter, M. P., ... & Moser, M. B. (2010). Development of the spatial representation system in the rat. *Science*, *328*(5985), 1576-1580.

Lisman, J., Buzsáki, G., Eichenbaum, H., Nadel, L., Ranganath, C., & Redish, A. D. (2017). Viewpoints: how the hippocampus contributes to memory, navigation and cognition. Nature neuroscience, 20(11), 1434-1447.

McNaughton, B. L., Barnes, C. A., & O'Keefe, J. J. E. B. R. (1983). The contributions of position, direction, and velocity to single unit activity in the hippocampus of freely-moving rats. *Experimental brain research*, *52*, 41-49.

Muller, R. U., Bostock, E., Taube, J. S., & Kubie, J. L. (1994). On the directional firing properties of hippocampal place cells. *Journal of Neuroscience*, *14*(12), 7235-7251.

Montaldi, D., & Mayes, A. R. (2010). The role of recollection and familiarity in the functional differentiation of the medial temporal lobes. *Hippocampus*, *20*(11), 1291-1314.

Maris, E., van Vugt, M., & Kahana, M. (2011). Spatially distributed patterns of oscillatory coupling between high-frequency amplitudes and low-frequency phases in human iEEG. Neuroimage, 54(2), 836-850.

Mullally, S. L., & Maguire, E. A. (2014). Memory, imagination, and predicting the future: A common brain mechanism?. The Neuroscientist, 20(3), 220-234.

Meister, M. L., & Buffalo, E. A. (2016). Getting directions from the hippocampus: The neural connection between looking and memory. Neurobiology of learning and memory, 134, 135-144.

Munn, R. G., Mallory, C. S., Hardcastle, K., Chetkovich, D. M., & Giocomo, L. M. (2020). Entorhinal velocity signals reflect environmental geometry. Nature neuroscience, 23(2), 239-251.

McNamee, D. C., Stachenfeld, K. L., Botvinick, M. M., & Gershman, S. J. (2021). Flexible modulation of sequence generation in the entorhinal-hippocampal system. Nat Neurosci, 24(6), 851-862. https://doi.org/10.1038/s41593-021-00831-7

Muhle-Karbe, P. S., Sheahan, H., Pezzulo, G., Spiers, H. J., Chien, S., Schuck, N. W., & Summerfield, C. (2023). Goal-seeking compresses neural codes for space in the human hippocampus and orbitofrontal cortex. Neuron.

Morris, G., & Derdikman, D. (2023). The chicken and egg problem of grid cells and place cells. Trends in Cognitive Sciences.

Naber, P. A., Lopes da Silva, F. H., & Witter, M. P. (2001). Reciprocal connections between the entorhinal cortex and hippocampal fields CA1 and the subiculum are in register with the projections from CA1 to the subiculum. Hippocampus, 11(2), 99-104.

Nichols, T. E., & Holmes, A. P. (2002). Nonparametric permutation tests for functional neuroimaging: a primer with examples. Hum Brain Mapp, 15(1), 1-25. https://doi.org/10.1002/hbm.1058

Nau, M., Navarro Schroder, T., Bellmund, J. L. S., & Doeller, C. F. (2018). Hexadirectional coding of visual space in human entorhinal cortex. Nat Neurosci, 21(2), 188-190. https://doi.org/10.1038/s41593-017-0050-8

Nyberg, N., Duvelle, É., Barry, C., & Spiers, H. J. (2022). Spatial goal coding in the hippocampal formation. Neuron.

O'Keefe, J., & Dostrovsky, J. (1971). The hippocampus as a spatial map: preliminary evidence from unit activity in the freely-moving rat. Brain research. https://doi.org/10.1016/0006-8993(71)90358-1

O'keefe, J., & Burgess, N. (2005). Dual phase and rate coding in hippocampal place cells: theoretical significance and relationship to entorhinal grid cells. Hippocampus, 15(7), 853-866.

Ormond, J., & O'Keefe, J. (2022). Hippocampal place cells have goal-oriented vector fields during navigation. Nature, 607(7920), 741-746.

Poppenk, J., Evensmoen, H. R., Moscovitch, M., & Nadel, L. (2013). Long-axis specialization of the human hippocampus. Trends in cognitive sciences, 17(5), 230-240.

Park, S. A., Miller, D. S., Nili, H., Ranganath, C., & Boorman, E. D. (2020). Map making: constructing, combining, and inferring on abstract cognitive maps. *Neuron*, *107*(6), 1226-1238.

Pfeiffer, B. E. (2020). The content of hippocampal "replay". Hippocampus, 30(1), 6-18.

Poulter, S., Lee, S. A., Dachtler, J., Wills, T. J., & Lever, C. (2021). Vector trace cells in the subiculum of the hippocampal formation. Nature neuroscience, 24(2), 266-275.

Qasim, S. E., Fried, I., & Jacobs, J. (2021). Phase precession in the human hippocampus and entorhinal cortex. Cell, 184(12), 3242-3255.

Rubin, A., Yartsev, M. M., & Ulanovsky, N. (2014). Encoding of head direction by hippocampal place cells in bats. Journal of Neuroscience, 34(3), 1067-1080.

Robinson, J. L., Barron, D. S., Kirby, L. A., Bottenhorn, K. L., Hill, A. C., Murphy, J. E., ... & Fox, P. T. (2015). Neurofunctional topography of the human hippocampus. Human brain mapping, 36(12), 5018-5037.

Rennó-Costa, C., & Tort, A. B. (2017). Place and grid cells in a loop: implications for memory function and spatial coding. Journal of Neuroscience, 37(34), 8062-8076.

Raithel, C. U., Miller, A. J., Epstein, R. A., Kahnt, T., & Gottfried, J. A. (2023). Recruitment of grid-like responses in human entorhinal and piriform cortices by odor landmark-based navigation. Current Biology, 33(17), 3561-3570.

Samsonovich, A., & McNaughton, B. L. (1997). Path integration and cognitive mapping in a continuous attractor neural network model. J Neurosci, 17(15), 5900-5920. https://www.ncbi.nlm.nih.gov/pubmed/9221787

Solstad, T., Moser, E. I., & Einevoll, G. T. (2006). From grid cells to place cells: a mathematical model. Hippocampus, 16(12), 1026-1031. https://doi.org/10.1002/hipo.20244

Sargolini, F., Fyhn, M., Hafting, T., McNaughton, B. L., Witter, M. P., Moser, M. B., & Moser, E. I. (2006). Conjunctive representation of position, direction, and velocity in entorhinal cortex. Science, 312(5774), 758-762.

Stam, C. J., Nolte, G., & Daffertshofer, A. (2007). Phase lag index: assessment of functional connectivity from multi channel EEG and MEG with diminished bias from common sources. Human brain mapping, 28(11), 1178-1193.

Sullivan, G.M., Feinn, R., 2012. Using effect size—Or why the P value is not enough. J.Grad. Med. Educ. 4 (3), 279–282. doi:10.4300/JGME-D-12-00156.1.

Stemmler, M., Mathis, A., & Herz, A. V. (2015). Connecting multiple spatial scales to decode the population activity of grid cells. Sci Adv, 1(11), e1500816. https://doi.org/10.1126/science.1500816

Schlichting, M. L., Mumford, J. A., & Preston, A. R. (2015). Learning-related representational changes reveal dissociable integration and separation signatures in the hippocampus and prefrontal cortex. Nat Commun, 6, 8151. https://doi.org/10.1038/ncomms9151

Stensola, T., Stensola, H., Moser, M. B., & Moser, E. I. (2015). Shearing-induced asymmetry in entorhinal grid cells. *Nature*, *518*(7538), 207-212.

Sarel, A., Finkelstein, A., Las, L., & Ulanovsky, N. (2017). Vectorial representation of spatial goals in the hippocampus of bats. *Science*, *355*(6321), 176-180.

Sun, Y., Jin, S., Lin, X., Chen, L., Qiao, X., Jiang, L., ... & Xu, X. (2019). CA1-projecting subiculum neurons facilitate object–place learning. Nature neuroscience, 22(11), 1857-1870.

Tolman, E. C. (1948). Cognitive maps in rats and men. Psychol Rev, 55(4), 189-208. https://doi.org/10.1037/h0061626

Taube, J. S., Muller, R. U., & Ranck, J. B. (1990). Head-direction cells recorded from the postsubiculum in freely moving rats. I. Description and quantitative analysis. Journal of Neuroscience, 10(2), 420-435.

Taube, J. S. (2007). The head direction signal: origins and sensory-motor integration. Annu. Rev. Neurosci., 30, 181-207.

Tsao, A., Moser, M. B., & Moser, E. I. (2013). Traces of experience in the lateral entorhinal cortex. Current biology, 23(5), 399-405.

Toledo, S., Shohami, D., Schiffner, I., Lourie, E., Orchan, Y., Bartan, Y., & Nathan, R. (2020). Cognitive map–based navigation in wild bats revealed by a new high-throughput tracking system. Science, 369(6500), 188-193.

Towers, Mark, Terry, Jordan K, Kwiatkowski, Ariel, Balis, John U., Cola, Gianluca, Deleu, Tristan, Goulão, Manuel, Kallinteris, Andreas, KG, Arjun, Krimmel, Markus, Perez-Vicente, Rodrigo, Pierré, Andrea, Schulhoff, Sander, Tai, Jun Jet, Tan, Andrew Jin Shen, & Younis, Omar G. (2023). Gymnasium (v0.29.0). Zenodo. https://doi.org/10.5281/zenodo.8148697

van Groen, T., Miettinen, P., & Kadish, I. (2003). The entorhinal cortex of the mouse: organization of the projection to the hippocampal formation. Hippocampus, 13(1), 133-149. https://doi.org/10.1002/hipo.10037

VanRullen, R., & Kanai, R. (2021). Deep learning and the Global Workspace Theory. Trends Neurosci, 44(9), 692-704. https://doi.org/10.1016/j.tins.2021.04.005

Witter, M. P., & Amaral, D. G. (1991). Entorhinal cortex of the monkey: V. Projections to the dentate gyrus, hippocampus, and subicular complex. J Comp Neurol, 307(3), 437-459. https://doi.org/10.1002/cne.903070308

Woolrich, M. W., Ripley, B. D., Brady, M., & Smith, S. M. (2001). Temporal autocorrelation in univariate linear modeling of FMRI data. Neuroimage, 14(6), 1370-1386. https://doi.org/10.1006/nimg.2001.0931

Wang, R. F., & Spelke, E. S. (2002). Human spatial representation: Insights from animals. *Trends in cognitive sciences*, *6*(9), 376-382.

Woolrich, M. W., Behrens, T. E., & Smith, S. M. (2004). Constrained linear basis sets for HRF modelling using Variational Bayes. Neuroimage, 21(4), 1748-1761. https://doi.org/10.1016/j.neuroimage.2003.12.024

Wills, T. J., Cacucci, F., Burgess, N., & O'Keefe, J. (2010). Development of the hippocampal cognitive map in preweanling rats. *science*, *328*(5985), 1573-1576.

Winter, S. S., & Taube, J. S. (2014). Head direction cells: from generation to integration. In Space, time and memory in the hippocampal formation (pp. 83-106). Vienna: Springer Vienna.

Welday, A. C., Shlifer, I. G., Bloom, M. L., Zhang, K., & Blair, H. T. (2011). Cosine directional tuning of theta cell burst frequencies: evidence for spatial coding by oscillatory interference. *Journal of Neuroscience*, *31*(45), 16157-16176.

Wilson, D. I., Langston, R. F., Schlesiger, M. I., Wagner, M., Watanabe, S., & Ainge, J. A. (2013). Lateral entorhinal cortex is critical for novel object-context recognition. *Hippocampus*, *23*(5), 352-366.

Whittington, J. C., Muller, T. H., Mark, S., Chen, G., Barry, C., Burgess, N., & Behrens, T. E. (2020). The Tolman-Eichenbaum machine: unifying space and relational memory through generalization in the hippocampal formation. *Cell*, *183*(5), 1249-1263.

Whittington, J. C., McCaffary, D., Bakermans, J. J., & Behrens, T. E. (2022). How to build a cognitive map. *Nature neuroscience*, *25*(10), 1257-1272.

Wagner, I. C., Graichen, L. P., Todorova, B., Lüttig, A., Omer, D. B., Stangl, M., & Lamm, C. (2023). Entorhinal grid-like codes and time-locked network dynamics track others navigating through space. Nature Communications, 14(1), 231.

Methods

Participants

Two groups of right-handed university students with normal or corrected-to-normal vision were recruited. The first group, which served as the experimental group, was 10 students from Peking University, and the second group contained ten students from Tsinghua University for replication purpose. Participants' age and sex were balanced between groups (experimental group: mean age = 22.10 [SD = 2.23], 5 females, 5 males; replication group: mean age = 23.9 [SD = 3.51], 5 females, 5 males). All participants had no history of psychiatric or neurological disorders and gave their written informed consent prior to the experiment, which was approved by the Research Ethics Committee of both universities.

Experimental design

Artificial object space. The greebles (Gauthier and Tarr, 1997) were created by 3ds Max (Autodesk, version 2022, http://www.autodesk.com) and the MAXScript codes from an open-source repository (TarrLab stimulus datasets, http://www.tarrlab.org/). The identity of individual greeble was determined by the lengths of its two components, named as "Loogit" and "Vacso" (Fig.1a, top). The names were arbitrary and had no relation to the object matching task (see below). We created 2025 greebles in total, each of which was equipped with a unique combination of Loogit's and Vacso's lengths. In this way, a 45-by-45 object space was constructed, with y-axis denoting Loogit's length and x-axis for Vacso's length (Fig. 1b). Therefore, in this 2-D artificial object space, each greeble represented a location. The greeble in the center of the space had equal length of Loogit and Vacso (i.e., prototype), which served as the target of the task. The ratio of a greeble parts' length over that of the prototype ranged from 0.12 to 1.88 with a step size of 0.04, which offered a smooth morphing experience when participants adjusted the length of object components.

Experimental procedure. In a trial of the object matching task, a greeble variant that was pseudo-randomly selected from greeble variants in the ring near the boundary of the space (red points in Fig.1b) was presented in the center of the screen after a 2.0-s fixation screen. Participants adjusted the lengths of the variant to match those of the prototype as quickly as possible by pressing buttons. There were four buttons, two of which were used to either stretching or shrinking one greeble part. When the participants felt that the adjusted variant completely matched the prototype, they either

pressed the return key to end the trial (self-pace in behavioral training) or waited the time limit to run out (fixed time limit in fMRI scan) (see below). To ensure paths from variants to the prototype covered most of locations in the space, 24 variants were randomly selected with its angular precision of 1° in each 30° bin of the ring, which made up 288 variants evenly distributed in the ring. The accuracy of a trial was indexed by the distance between prototype's location and the location where the participant stopped. To encourage the participants to perform the task as accurately as possible, participants were informed that the amount of their monetary compensation increased exponentially with their performance. The task was programmed by Python (version 3.9) and Pygame (a library designed for writing video games, version 2.0, https://www.pygame.org/).

The task was conducted twice in two consecutive days, one for behavioral training and the other for fMRI scan. On day 1, the participants adjusted the length of variant's parts to match the prototype in a self-paced fashion. There were 8 sessions with 36 trials each, which made up 288 trials in total and took about 1 hour. The first 7 sessions provided feedback at the end of trials (e.g., "Loogit: 5 percent longer than the target") and the 8th session had no feedback for measuring behavioral performance. Before the training, the participants learned the prototype by watching it on the screen, and then performed at least 10 trials with feedback as practice. On day 2, the procedure was identical to that of day 1, except that (1) the self-pace was replaced with a 10-s time limit for each trial with a timer presented on top of screen (Fig.1b), (2) no feedback was provided for all sessions, and (3) the participants finished the experiment in fMRI scanner. After the fMRI scan, the participants were debriefed, and none was aware of the existence of the object space or the analogy of the adjustment of the length of object components during path integration. The behavioral performance of participants that fluctuates as a function of conceptual directions was defined by $0.04 \times T + E$, where T represents the length of trajectory, denoting the movement steps, which was scaled into the distance of object space by a constant parameter 0.04, E denotes the error, quantified by the distance between the goal location and the location participants stopped in object space.

fMRI data acquisition

Imaging data were collected using a 3T Siemens Prisma scanner equipped with a 64- and 20-channel receiver head coil for the experimental group and replication group at PKU and Tsinghua

Imaging Center, respectively. Functional data were acquired with a Multi-band Echo Planer imaging (EPI) sequence (TR = 2000 ms, TE = 30 ms, matrix size: 112 × 112 x 62, flip angle: 90°, resolution: 2 × 2 × 2.3 mm^3, number of slices: 62, slice thickness: 2 mm, gap = 0.3 mm, slice orientation: transversal). A high-resolution T1-weighted three-dimensional anatomical data set was collected for registration (MPRAGE, TR = 2530 ms, TE = 2.98 ms, matrix size: 448 x 512 x 192, flip angle: 7°, resolution: 0.5 × 0.5 × 1 mm3, number of slices: 192, slice thickness: 1 mm, slice orientation: sagittal). In the experimental group, stimuli were presented through a Sinorad LCD projector (Shenzhen Sinorad Medical Electronics) onto a 33-inch rear-projection screen. In the replication group, the stimuli were presented using a visual/audio stimulation system (Shenzhen Sinorad SA-9939) with a customized-design (Shenzhen Sinorad Medical Electronics Co., Ltd) MRI compatible 40" LED liquid crystal display. The resolution of screens was 1024 x 768, and the participants viewed the stimuli with an angled mirror mounted on the head coil.

fMRI data preprocessing

The BOLD time series of each scan session was preprocessed independently using FSL FEAT toolbox (FMRIB's Software Library, version 6.0, https://fsl.fmrib.ox.ac.uk/fsl/fslwiki; Woolrich et al. 2001; Woolrich et al. 2004). For each session, the time series were corrected for motion artifacts, slice time acquisition differences, geometrical distortion using the fieldmaps, and were high-pass filtered at 100 s. Spatial smoothing was further applied using a 5 mm FWHM Gaussian kernel. For group-level statistics, each session's functional data were registered to participant's high-resolution anatomical image and were then normalized to a standard image (MNI152) using FSL FLIRT (Jenkinson and Smith, 2001). This procedure also resampled the functional voxels into a 2 x 2 x 2 mm resolution.

Sinusoid analysis

To test whether the hexagonal pattern was present during the object matching task, we first computed the hexagonal orientation in the ERC for each participant using one half of the data (odd-numbered sessions). Second, we looked for the hexagonal pattern that was modulated by participants' spatial orientation ranging from 0° to 360° in the object space after controlling for the effect of hexagonal orientation (Doeller et al., 2010; Constantinescu et al., 2016; Bao et al., 2019; Wagner et al., 2023; Raithel et al., 2023). Specifically, a GLM was created for each session

to model the time series convolved with FSL Double-Gamma hemodynamic response function in the ERC with two parametric modulators: sin(6θ) and cos(6θ), where θ represents the spatial-orientation in the object space. The factor 6 means the 6-folded neural activity, which is rotational symmetric and aligned with spatial-orientation. The factor 5 and 7 were used as controls, which misaligned with the hexagonal pattern. Those estimated parameters β_{sine} and β_{cosine} were subsequently used to compute the hexagonal orientation φ, ranged from 0° to 59°, in each voxel and each participant, where $\varphi = [\arctan(\frac{\beta_{sine}}{\beta_{cosine}})]/6$. The hexagonal orientation Φ for each participant was derived by averaging the φ map across the odd-numbered sessions and voxels in the ERC. Once the hexagonal pattern of neural activity in the ERC was identified, a second GLM was fitted to model the BOLD signal series from the other half of the data (even-numbered sessions), which was specified by a cosine parametric modulator: cos(6[θ - Φ]). The activity map of the hexagonal pattern was derived by averaging the parametric map of this cosine modulator across the even-numbered sessions, which was further converted to z-score map before submitting to second-level analysis (Schlichting et al., 2015).

Spectral analysis of MRI BOLD signals

To examine the spectrum of BOLD signal series within the MTL, we created a GLM to extract the activity map corresponding to each movement direction in the object space, and then performed voxel-based spectral analyses to identify robust periodic activity. Specifically, the movement directions, which were represented by the trajectories from variants to the prototype, were first down-sampled into bins with 15° each (e.g., the movement directions within -7.5° to 7.5°was label as 0° and the movement directions within 337.5° to 352.5°was label as 345°). This procedure resulted in a vector of 24 resampled movement directions (i.e., the number of bins), which was sufficient samples for spectral analysis (De Valois et al., 1982) and was used to look for the spatial periodicity of neural activity ranged from 0Hz to 11Hz. Next, the BOLD signal series in correspond to the movement directions was modelled by a GLM with the directional bins specified as parametric modulators, producing the movement direction-dependent activity maps for each participant, which were extracted from each voxel of the MTL, and were sorted in ascending order (i.e., 0° to 345°). Next, we performed the spectral analysis on the BOLD signal series using the Fast Discrete Fourier Transform (FFT) included by the stats package of R platform (version 4.0, https://www.r-project.org/; Landau and Fries, 2012), where the detrending, Hanning tapper, and

zero-padding were applied for preprocessing. The BOLD signal series was then converted into frequency domain from spatial domain, and the spectrum magnitude was derived by computing the absolute values of the complex FFT output. This procedure generated a brain map of magnitude for each frequency. The 95th percentile of pseudo t-statistic distribution (the mean magnitude divided by the SE across participants) was computed as the initial threshold for each voxel of the MTL for second-level analysis.

Anatomical masks

We manually delineated the bilateral ERC for ROI analyses on the MNI T1 brain with 2 mm resolution packaged by FSL using established protocols (Insausti et al. 1998), as well as a delineating software ITK-SNAP (Version 3.8, www.itksnap.org). The masks of HPC subfields were derived by an automated segmentation tool packaged by Freesurfer (Version 7.1, https://surfer.nmr.mgh.harvard.edu/; Iglesias et al., 2015), which segments the CA1 and CA2/3 area from hippocampal formation and further divides the mask into head and body parts. All masks were resampled to 2 mm resolution and aligned in standard MNI space.

The "R-H PhaseSync" model

The model, implemented using Python (version 3.9), was hypothesized to elucidate the mechanism of the formation of the 3-fold periodicity observed in the HPC. The agent was programmed to perform path integration on a 45-by-45-pixel space, where each spatial location (1 out of 2025 pixels) was denoted by the coordinate vector $r = (x, y)$ with the goal-location located in the center of space ($r = (22,22)$). The model hypothesizes the movement direction embedded by the hippocampal vector field relying on the signal projection of entorhinal grid cells. Specifically, the grid cell populations activated by path planning send the hexagonal representations to the downstream areas (Witter & Amaral, 1991; van Groen et al., 2003; Fyhn et al., 2007; Hales et al., 2014; Garcia and Buffalo, 2020), where the vector trace cells in the subiculum, which were known to represent sequential locations of object (Tsao et al., 2013; Bicanski & Burgess, 2018; Bicanski & Burgess, 2020; Poulter et al., 2021), encode spatial orientations embedded by the three-fold periodicity of populational hexagonal codes. Hippocampal place cells then inherit the three-fold scaffold to structure movement directions using multi-scale encoding. Finally, the vector field can be generated by place cell population with distance binding. The model conforms with the winner-

take-all dynamics for path integration (Bicanski & Burgess, 2019), which looks for the location with the strongest neural activity surrounding to self-location until the goal is approached (Ormond & O'Keefe, 2022).

Simulation of Entorhinal Grid cell. Grid cell populations were generated by the cosine grating model (O'keefe and Burgess, 2005; Burgess et al., 2007; Blair et al., 2007; Bush and Schmidt-Hieber, 2018). For single cell, the spatial code G at spatial location $r_{(x,y)}$ was derived by summing three cosine gratings under the spatial phase $c_{(x_0,y_0)}$ (Equation 4). The cosine gratings were oriented by the rotation vector k with 60° apart from one another. The parameter A denotes the amplitude of cosine gratings. Four spatial scales of grid cell (i.e., denoted by grid module Ω) were generated for each spatial location $r_{(x,y)}$ to achieve the multi-scale representation of space. The scale-ratio of grid modules was defined at approximately 1.4 according to previous model simulations (Kang and Balasubramanian, 2019; Killian et al., 2012; Stemmler et al., 2015). This procedure generated a total of 2024 grid cells for each grid module, where grid orientations were consistent, and grid phases were varied.

$$G_r = \sum_{i=1}^{3} A\cos(\omega_i(k_{i,x}(r_x - c_x) + k_{i,y}(r_y - c_y))) \tag{4}$$

Simulation of subiculum vector trace cell. Vector trace cell (VTC) populations were simulated using the conjunctive representation of grid cells activated by path planning (Fig.3a & b, Buckner, 2010; Mullally and Maguire, 2014; Lisman et al., 2017; Whittington et al., 2022). For single VTC, the trace field V was denoted as exp $(\sum_i^k G_i)$, where G denotes the grid code, i and k denote the starting- and goal-location, respectively. Previous studies have indicated the property of VTC in encoding sequential locations of objects (Tsao et al., 2013; Bicanski & Burgess, 2018; Bicanski & Burgess, 2020; Poulter et al., 2021). Correspondingly, we assumed VTCs in our model encoding the sequential locations of self-body during path planning. Given the symmetry of object space, the trace field V is symmetrical for the movement direction φ_i and the direction $\varphi_{i+180°}$ (Fig.3c), naturally reflecting the spatial orientation ψ of object space (Fig. 3d). In this case, the space can be tessellated by VTC population, which encodes the spatial orientation ranged from 0 to π.

$$\delta_r = \begin{cases} \Psi_{\max,\mathrm{r}} - (\phi_r \mod \pi) & \text{if } \Psi_{\max} > \Psi_{\mathrm{mean}} + 2\sigma \\ 1 & \text{otherwise} \end{cases} \tag{5}$$

The activity of VTC cells was quantified by how closely the encoded spatial orientation aligned with the corrected movement direction ϕ_r (Equation 5), a process similar to the determination of head directions (Taube et al., 1990; Johnson et al., 2005 ; Taube, 2007; Winter and Taube, 2014). Specifically, we decoded the spatial orientation ψ for each location by building the activity vector Ψ, where the activity of each ψ was computed by summing the trace values of V across the locations oriented at the orientation ψ. The maxima of Ψ was identified using the find_peaks function (Scipy, version 1.9.3). Ψ_{max} was then defined as the encoded orientation if its trace value exceeded the threshold defined in Equation 5. Otherwise, the constant value of one was assigned to location r. Next, the spatial orientations of VTC population were compared with movement direction ϕ_r, resulting the two-dimensional matrix δ, which was normalized into the ranger of 0 to 1 to represent the activity strength of VTC cells (Equation 6).

$$\delta_{\mathrm{normalized}} = 1 - \frac{\delta_r - \delta_{\min}}{\delta_{\max} - \delta_{\min}} \tag{6}$$

Simulation of Hippocampal vector field. The vector field C was constructed by integrating the spatial representation of movement direction $C_{Direction}$ and the spatial representation of distance $C_{Location}$ (Equation 2). Both $C_{Direction}$ and $C_{Location}$ denote a two-dimensional activity matrix averaged across Ω. $C_{Direction}$ was defined by a cosine function with the frequency f_δ and the phase θ_δ inherited from the VTC space δ (Equation 3), where the neural activity fluctuated as a function of spatial orientation. r'_x and r'_y denotes the location shifts relative to the goal-location. The term arctan $(\frac{r'_y}{r'_x})$ denotes a two-dimensional matrix of movement directions, which were ranged from 0° to 360°, relative to the goal in environmental center. $C_{Location}$, which is insensitive to movement directions but encode the distance between self- and goal-location, is defined by a Q-value map from training a standard RL model over the two-dimensional space using Gymnasium library (OpenAI, version=0.29; Towers et al., 2023).

During simulation, a total of 156 locations, forming a ring-shaped pattern near the boundary of space, serve as the starting locations.. In each movement step, a vector of neural activity from the locations surrounded by self-location was extracted from C, the agent moved to the location with the strongest activity to approach one transition. During this process, the step size was adapted to a stepwise approach. That is, the initial step size of 1 pixel was used. The step size was increased by 1 pixel if no stronger activity was found from the surrounding locations. The coordinate sequences between the starting- and the goal-location were recorded during the simulation, the travel length was computed by the sum of the distances of every location-pairs. The vector of travel lengths across movement directions were then sorted with ascending order before submitting to spectrum analysis.

Statistical analysis

The 3-fold and 6-fold neural periodicity were examined by cluster-based permutation using FSL randomise package (version 2.9, http://fsl.fmrib.ox.ac.uk/fsl/fslwiki/Randomise), where an initial threshold of $p < 0.01$ was used to derive the uncorrected clusters. If no clusters were revealed, a liberal threshold of $p < 0.05$ was used. The reliability of the uncorrected clusters was further tested using a non-parametric statistical inference that does not make assumptions about the distribution of the data (Nichols and Holmes 2002). Specifically, 1,000 random sign-flips were performed on the beta or FFT magnitude images. The clusters with size higher than 95% of the maximal suprathreshold clusters from permutation distribution were reported. The periodicity of behavioral performance recorded from human participants and the "E-H PhaseSync" model was examined using FFT, where the initial threshold of each frequency was derived from the 95% percentile of shuffled magnitude distribution, the threshold corrected for multiple comparison was selected by the maximum of the initial thresholds across frequencies. The coherence between the BOLD signal series of the ERC and HPC and between the BOLD signal series of HPC and task performance series in conceptual directions was examined using the amplitude-phase coupling analysis (Canolty et al., 2006) and the phase-lag index analysis (Stam et al., 2007), respectively. Note that no band-passed filter was applied to either the ERC or HPC BOLD signal series. The robustness of coherence was evaluated by permutation test with 1000 shuffling applied on the conceptual directions. The coherence that higher than the top 5% of shuffled distribution was considered to be significant. All the t-tests used in the present study were two-tailed.

1278

Supplemental Material

“Spatial periodicity of hippocampal place cells in navigation”

Bo Zhang and Jia Liu

Figure S1. Behavioral results of the human participants from the experimental and replication group. The error was defined as the distance between the prototype location and the location where the participants stopped. On day 1, the task errors decreased as a function of experimental sessions, resulting a significantly negative slope for both groups of participants (experimental group: $t(9) = -3.90$, $p = 0.003$; replication group: $t(9) = -2.82$, $p = 0.019$). No significant learning effect was found during the MRI scan of day 2 (experimental group: $t(9) = -0.22$, $p = 0.834$; replication group: $t(9) = -0.10$, $p = 0.922$). This design ruled out the possibility of learning effect in examining the neural periodicity within the MTL. Error bars indicate SEM.

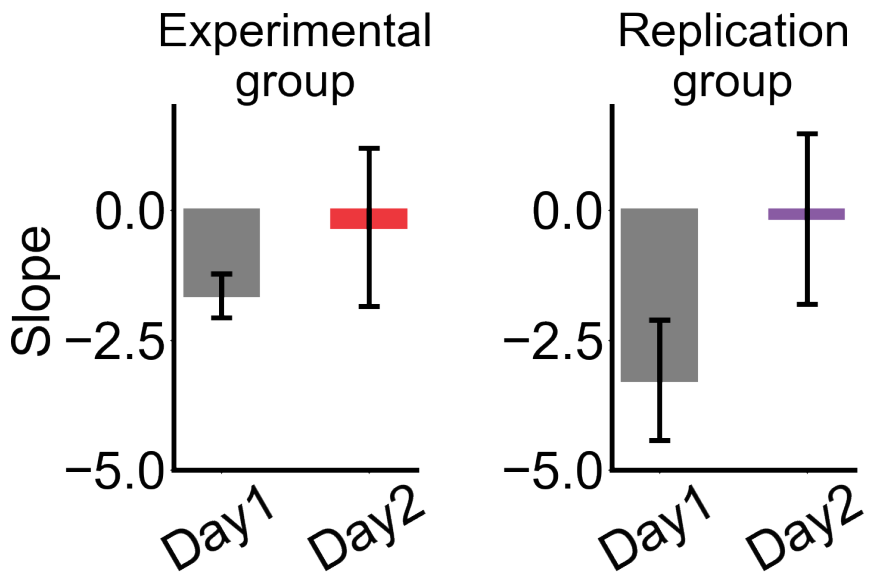

Figure S2. Trajectories of human participants recorded during MRI scanning. The orange dots denote the start locations while the red/purple dots indicate the end locations for the experimental (red) and replication (purple) group.

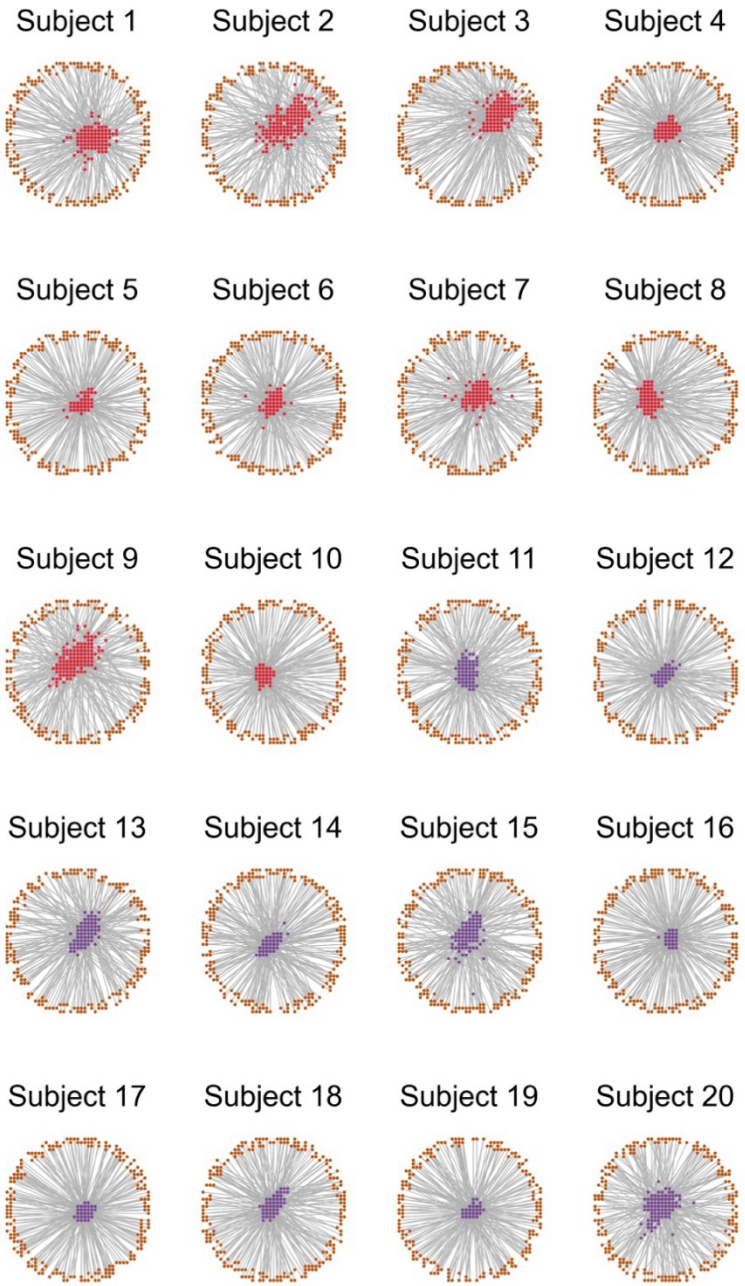

Figure S3. Distribution of hexagonal orientations in the ERC of the experimental (red) and replication (purple) group. The uniformity of hexagonal orientations, which was computed from each voxel, was tested by Rayleigh test. All participants showed significantly clustered hexagonal orientations ($p < 0.05$, Bonferroni corrected). The length of bars indicates the number of voxels and the black line denotes the mean of hexagonal orientations.

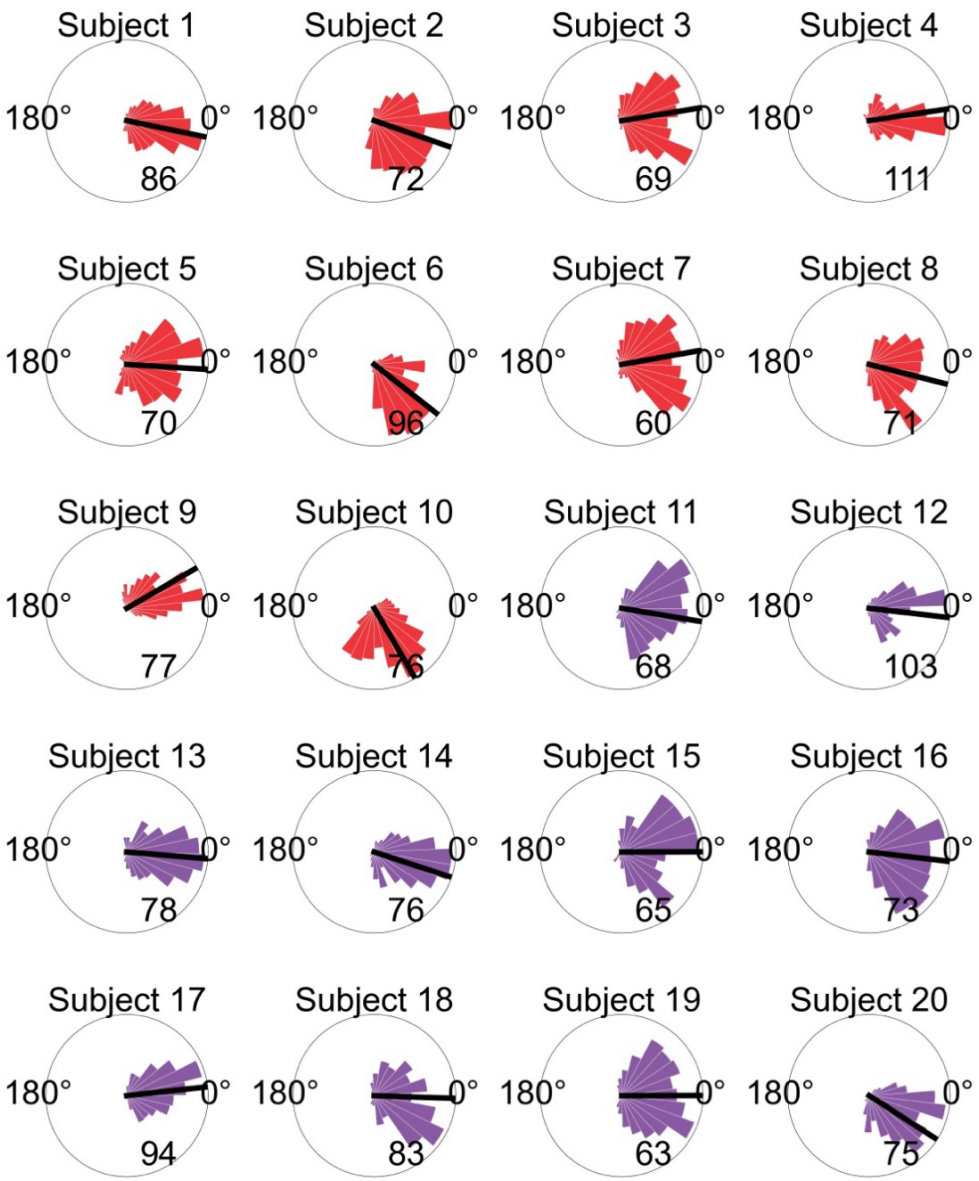

Figure S4. The 3-fold modulation of the HPC examined using 10° and 20° bin. The significant clusters were robustly revealed in the right HPC (initial threshold on pseudo t-value: $p < 0.05$; SVC for multiple comparison: $p < 0.05$). The x & y value denote MNI coordinate.

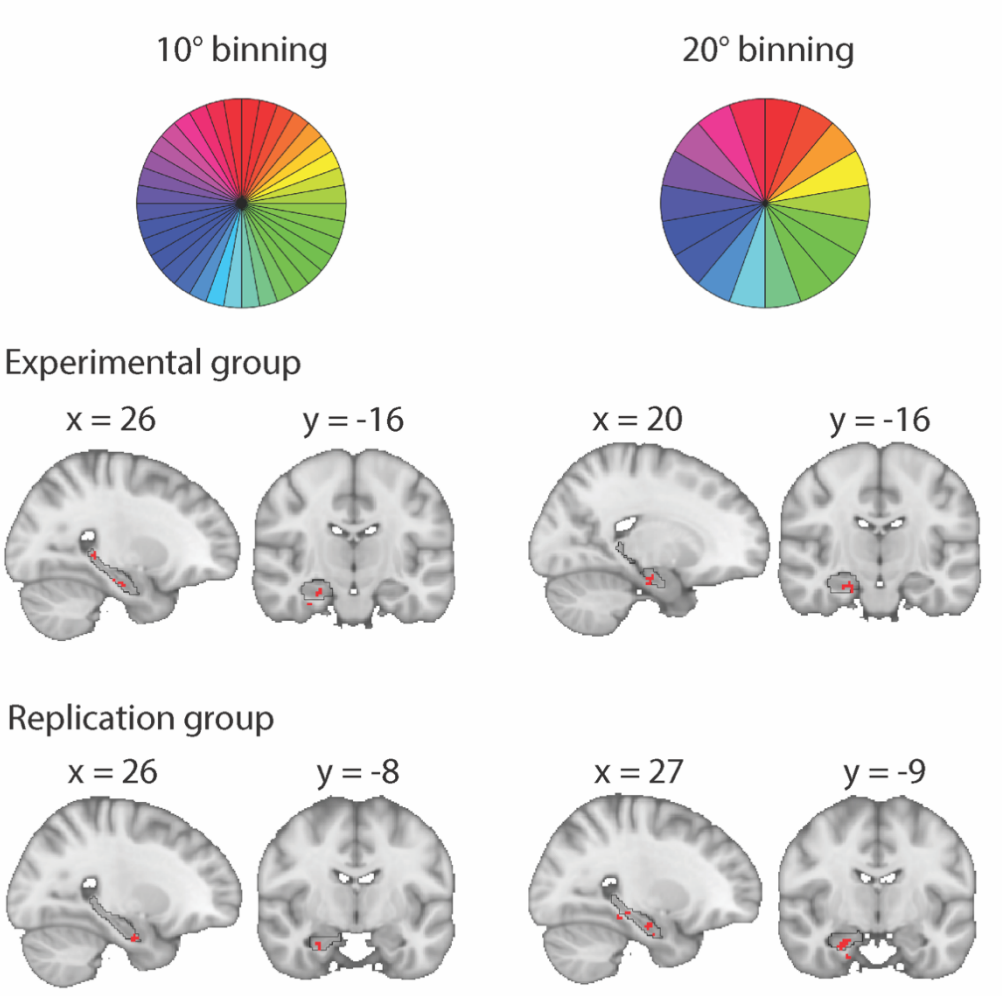

Figure S5. Neural periodicity of the ERC and the HPC observed in the replication group. The 6- and 3-fold modulation, revealed by sinusoid and spectral analysis, was revealed in the right ERC and the right HPC, respectively (initial threshold: $p < 0.01$; SVC for multiple comparisons: $p < 0.05$). Error bar denotes SEM.

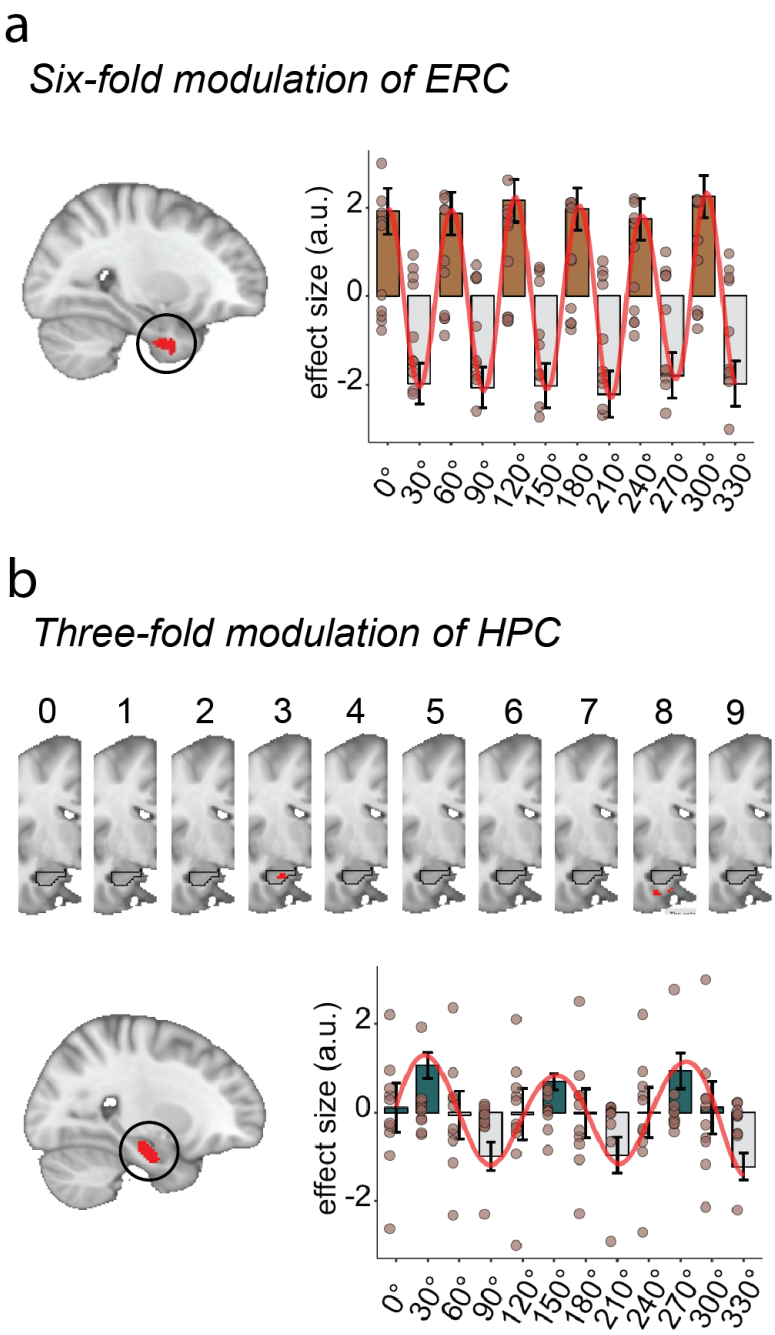

Figure S6. BOLD signal series of the ERC (black) and HPC (red & purple denoting the experimental and replication group, respectively) fluctuate as a function of conceptual directions (0°-360°; shown on x-axis).

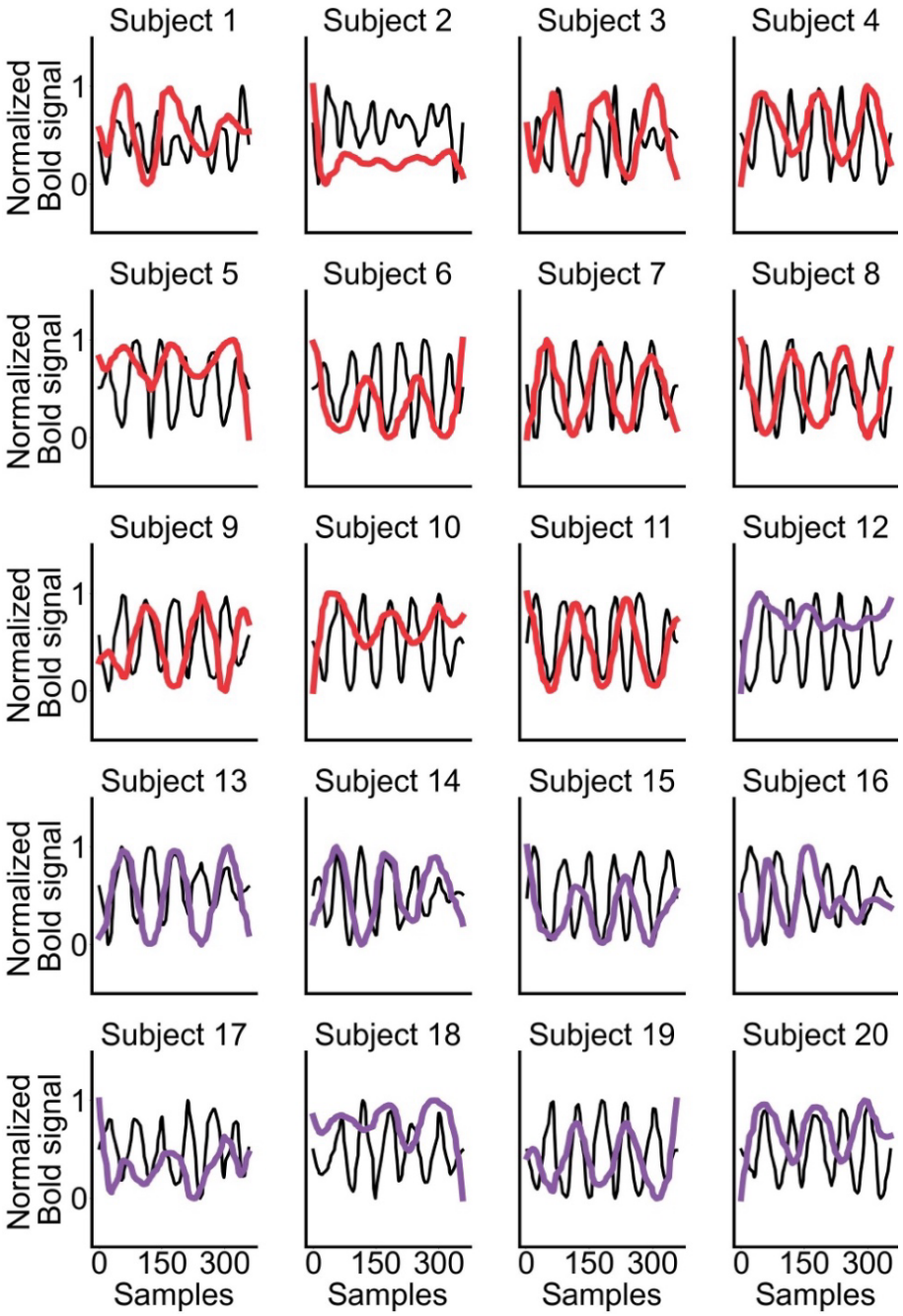

Figure S7. Schema of the three-fold scaffold encoded by the subiculum embedding the movement directions encoded by the HPC using multi-scale encoding. The red circle and arrow indicate spatial phase precession, the phase that embedding the 4th movement direction moves toward zero with the number of neurons, denoted by N, increases.

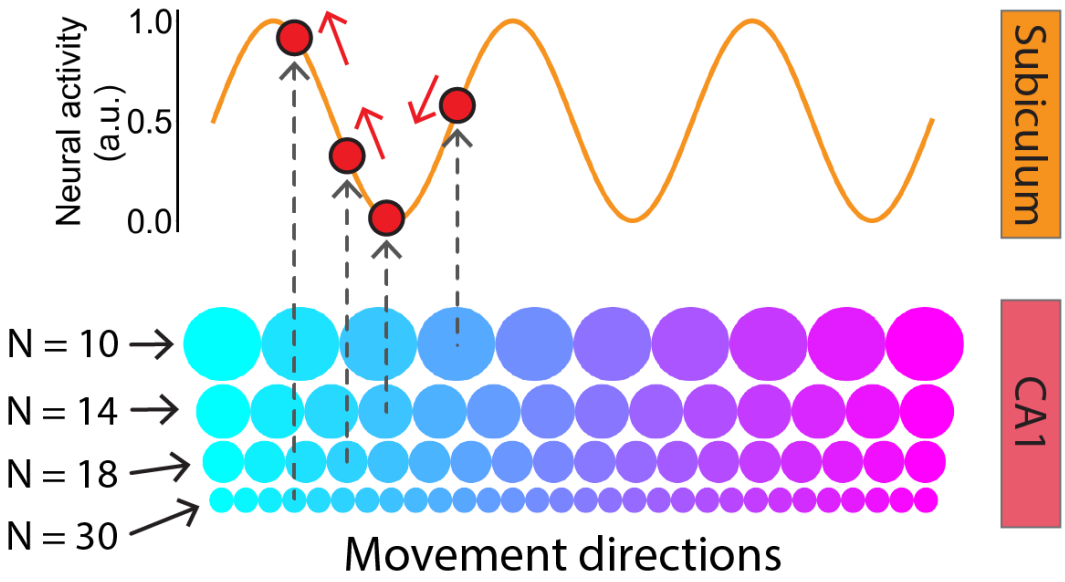
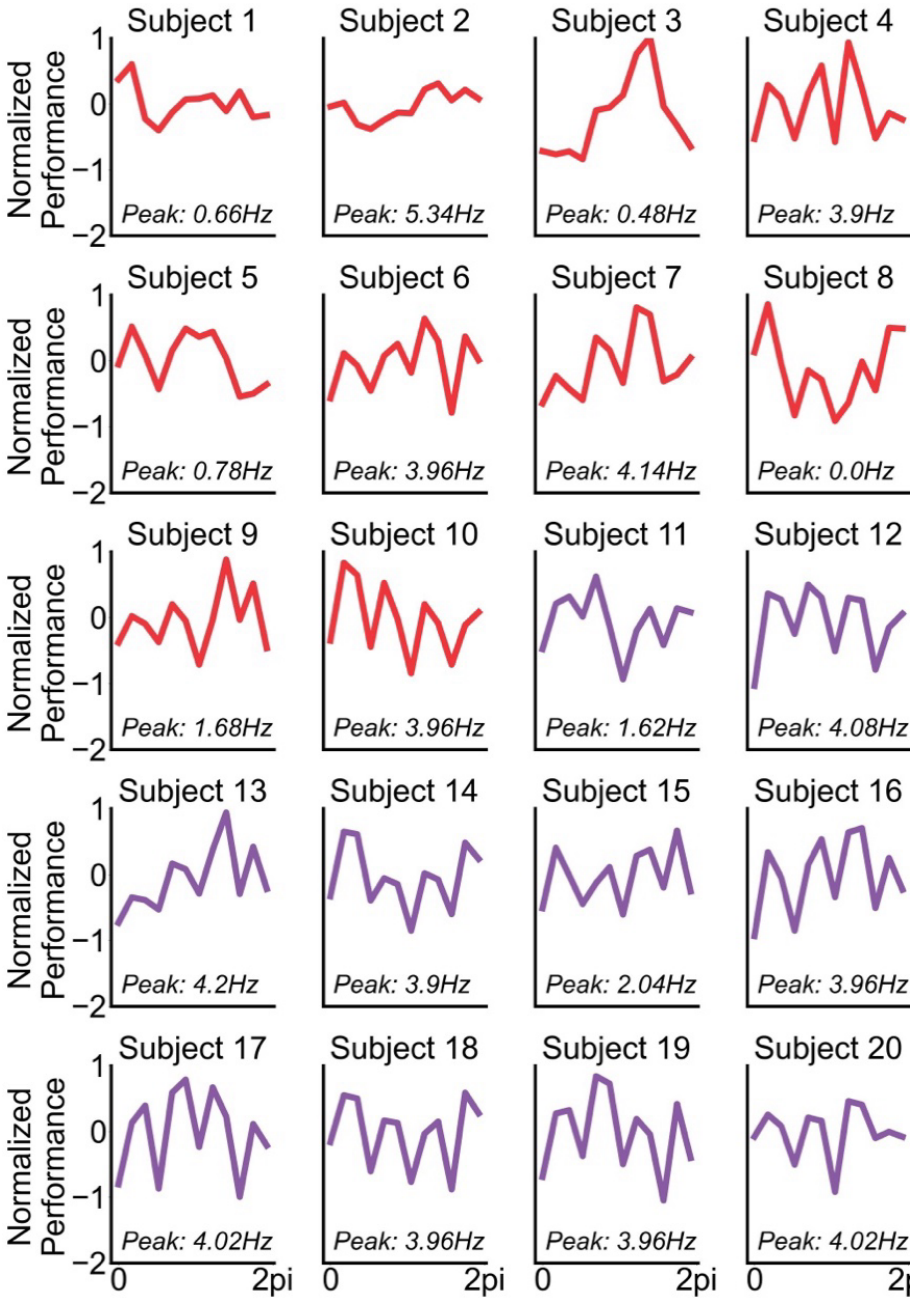
Figure S8. Raw behavioral performances of human participants from the experimental (red) and replication (purple) group change as a function of conceptual directions (0 to 2pi shown on x-axis).